

CONTENT

Vol. 8. No. 1-2022

Rui J. P. de Figueiredo and Byung Moo Lee

A New Pre-Distortion Approach to TWTA
Compensation for Wireless OFDM Systems

2

Slawomir Koziel

Noise Analysis and Optimization of General
OTA-C Filters

7

**Romeo Ghinea, Liviu Goras,
Michael Ansoerge, Tecla Goras**

Nonideal Behaviour of OA-Based Astable Multivibrators
with Applications in Linear Capacitance-
and Inductance-to-Time Conversions

14

Chin-Teng Lin, Jen-Feng Chung, and Der-Jenq Liu

A programmable DSP core design
for speech/audio codec SOC

20

Byung Moo Lee and Rui J. P. de Figueiredo

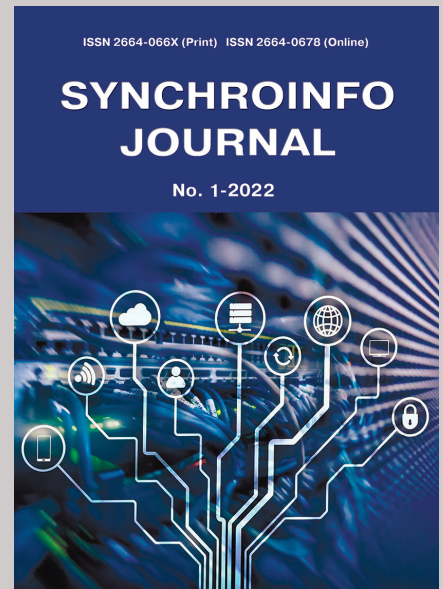
BLAST Performance in MIMO Wireless
Communication Systems

25

Svetlana Dymkova

Earth Observation and Global Navigation Satellite Systems
Analytical Report PART I (AVIATION AND SPACE)

30



Published bi-monthly since 2015.

*ISSN 2664-066X (Print)
ISSN 2664-0678 (Online)*

Publisher

Institute of Radio and
Information Systems (IRIS),
Vienna, Austria

Deputy Editor in Chief

Albert Waal (*Germany*)

Editorial board

Oleg V. Varlamov (*Austria*)

Corbett Rowell (*UK*)

Andrey V. Grebennikov (*UK*)

Eric Dulkeith (*USA*)

German Castellanos-

Dominguez (*Colombia*)

Marcelo S. Alencar (*Brazil*)

Ali H. Harmouch (*Lebanon*)

Address:

*1010 Wien, Austria,
Ebendorferstrasse 10/6b
media-publisher.eu/
synchroinfo-journal*

© Institute of Radio and Information
Systems (IRIS), 2022

A NEW PRE-DISTORTION APPROACH TO TWTA COMPENSATION FOR WIRELESS OFDM SYSTEMS

*Rui J. P. de Figueiredo and Byung Moo Lee,
Laboratory for Intelligent Signal Processing and Communications
University of California, Irvine
rui@uci.edu, byungl@uci.edu*

DOI: 10.36724/2664-066X-2022-8-1-2-6

ABSTRACT

Orthogonal Frequency Division Multiplexing (OFDM) has several desirable attributes which makes it a prime candidate for a number of emerging wireless communication standards. However, one of the major problems posed by OFDM is its high Peak-to-Average-Power ratio (PAPR), which seriously limits the power efficiency of the High Power Amplifier (HPA) because of the nonlinear distortion resulting from high PAPR. The present paper presents a new mixed computational/analytical approach for compensation of this nonlinear distortion for the case in which the HPA is a Traveling Wave Tube Amplifier (TWTA) with time-varying characteristic. TWTAs are used in wireless communication systems when high transmission power is required as in the case of the digital satellite channel. Compared to previous pre-distorter techniques based on LUT (Look-Up Table) or adaptive schemes, our approach relies on the analytical inversion of the Saleh TWTA model in combination with a nonlinear parameter estimation algorithm. This leads to a sparse and yet accurate representation of the pre-distorter, with the capability of tracking efficiently any rapidly time-varying behavior of the TWTA. Computer simulations results illustrate and validate the approach presented.

KEYWORDS: *Orthogonal Frequency Division Multiplexing, OFDM, Traveling Wave Tube Amplifier, TWTA.*

The article is reworked from unpublished 2nd IEEE International Conference on Circuits and Systems for Communications (ICCSC) materials.

I. INTRODUCTION

Orthogonal Frequency Division Multiplexing (OFDM) has several desirable attributes, such as high immunity to inter-symbol interference, robustness with respect to multi-path fading, and ability for high data rates, all of which are making OFDM to be incorporated in emerging wireless standards like IEEE 802.11a WLAN and ETSI terrestrial broadcasting. However, one of the major problems posed by OFDM is its high Peak-to-Average-Power Ratio (PAPR), which seriously limits the power efficiency of the High Power Amplifier (HPA) because of the nonlinear distortion caused by high PAPR. This distortion constitutes a source of major concern to the RF system design community. One of the most promising approaches for the mitigation of this nonlinear distortion is to use a Pre-Distorter, applied to the OFDM signal prior to its entry into the HPA. Except for Brajal and Chouly, previous Pre-Distorter-based approaches consisted of: (1) Using a Look-Up Table (LUT) and updating the table via Least Mean Square (LMS) error estimation [1] [2]; (2) two-stage estimation, using Wiener system modeling for the HPA, and Hammerstein system modeling for the pre-distorter [3]; (3) simplified Volterra-based modeling for compensation of the HPA nonlinearity. [4] [5]; and (4) polynomial approximation of this nonlinearity [6]. However, all of these techniques are based on a general approximation form for the nonlinear system, rather than on exploiting specific forms gleaned from physical device considerations.

In the present paper, we describe a new approach to PD (pre-distorter) for TWTA by using the Saleh model for this device and using the exact closed form expression for its inverse represented by means of only four parameters, thus avoiding a larger number of parameters that a generic approximation expression (like the polynomial approximation) would require for accurate representation. Brajal and Chouly [9] did present a closed form expression for the inverse for the Saleh model [7] but did not use this inverse in the implementation of their Pre-Distorter for the case of in which the characteristic of the TWTA is time-varying.

We have combined the closed form expression for the inverse of the TWTA characteristic with a sequential nonlinear parameter estimation algorithm, which allows sparse implementation of the PD and accurate tracking of the time varying behavior of the TWTA.

II. SYSTEM DESCRIPTION

Fig.1 shows a simplified block diagram for compensation of the HPA nonlinearity for OFDM system. Typically, OFDM signal can be represented as

$$x(t) = \frac{1}{\sqrt{N}} \sum_{k=0}^{N-1} X[k] e^{j2\pi f_k t} \quad (1)$$

where $X[k]$ denotes QAM symbol, N is the number of subcarriers, and f_k is k^{th} subcarrier frequency which can be represented as

$$f_k = k \cdot \frac{1}{NT_s} \quad (2)$$

where T_s is symbol duration of $x(t)$.

By discretizing $x(t)$ at $t = nT_s$, we have the following equation

$$x(n) \equiv x(nT_s) = \frac{1}{\sqrt{N}} \sum_{k=0}^{N-1} X[k] e^{j\frac{2\pi k n}{N}} \quad (3)$$

As a HPA model, we use Saleh's well established TWTA model. In this model, AM/AM and AM/PM conversion of TWTA can be represented as [7]

$$u[r] = \frac{\alpha r}{1 + \beta r^2} \quad (4)$$

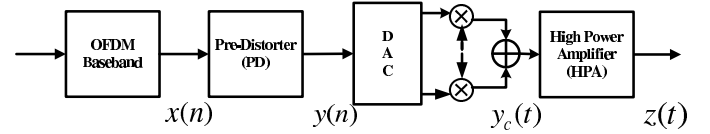


Fig. 1. Simplified OFDM Transmitter with PD and HPA

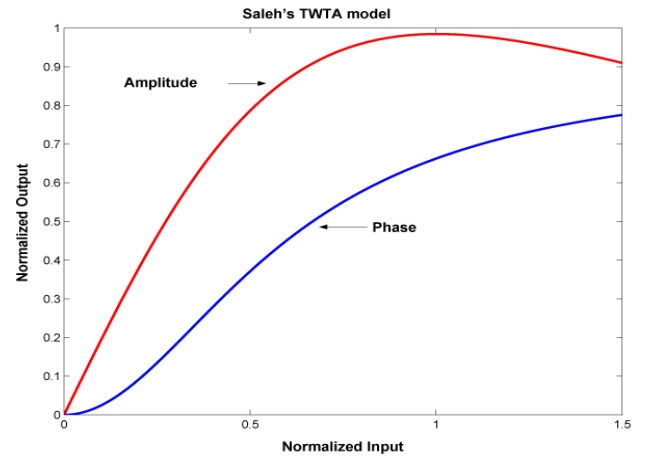


Fig. 2. Nonlinear amplitude and phase transfer function of the Saleh's TWTA model

$$\Phi[r] = \frac{\gamma r^2}{1 + \varepsilon r^2} \quad (5)$$

where r is input amplitude of TWTA and $\alpha, \beta, \gamma, \varepsilon$ are four adjustable parameters. The behavior of (4) and (5) is illustrated in Fig.2. In this figure we use $\alpha = 1.9638, \beta = 0.9945, \gamma = 2.5293, \varepsilon = 2.8168$ as in Saleh's original work [7] The output of TWTA without PD can be represented as

$$z(t) = u[r] \cos(\omega_c t + \varphi(t) + \Phi[r]) \quad (6)$$

where $\theta(t)$ is the phase of the input signal.

III. PRE-DISTORTER

Let g and h denote the nonlinear zero memory input output maps of the PD and HPA, and $x(t)$, the input of the PD, $y(t)$, the output of the PD which is also the input to the HPA, and $z(t)$ the output of the HPA as in Fig 1. Then for any given HPA, an ideal pre-distorter is one for which the input-output maps satisfy

$$h[g(x(t))] = k \cdot x(t) \quad (7)$$

where k is a desired pre-specified linear amplification constant. In this paper, we assume $k = 1$.

According to [9], the PD for amplitude compensation which satisfy (7) is

$$q(r) = \frac{\alpha - \sqrt{\alpha^2 - 4r^2\beta}}{2r\beta}, \quad r \leq 1 \quad (8)$$

Also for zero phase distortion, we must have

$$\theta(r) + \Phi(q) = 0 \quad (9)$$

or

$$\theta(r) = -\Phi(q) = -\frac{\gamma(q(r))^2}{1 + \varepsilon(q(r))^2} \quad (10)$$

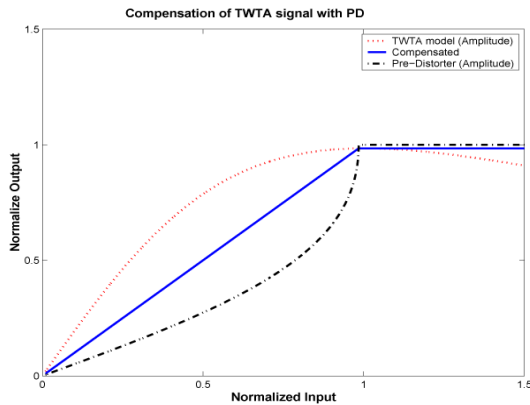


Fig. 3. Amplitude compensation effect of Saleh's TWTA model

If $r > 1$, equation (8) has no solution. In this case, we clip the signal as in Fig 3. This analytical solution (8), (10) was previously obtained by Brajal and Chouly [9]. We now extend this solution to the time-varying as follows.

We express MSE in amplitude as

$$J(\alpha, \beta) = E \left(\frac{\alpha q}{1 + \beta q^2} - u \right)^2 \quad (11)$$

Partially differentiating w. r. t. α and equating the result to zero, we get,

$$\frac{\partial J(\alpha, \beta)}{\partial \alpha} = E \left[2 \left(\frac{\alpha q}{1 + \beta q^2} - u \right) \frac{q}{1 + \beta q^2} \right] = 0 \quad (12)$$

$$\alpha E \left(\frac{q^2}{(1 + \beta q^2)^2} \right) = E \left(\frac{qu}{1 + \beta q^2} \right) \quad (13)$$

Differentiating (11) w. r. t. β and equating the result to 0,

$$\frac{\partial J(\alpha, \beta)}{\partial \beta} = E \left[2 \left(\frac{\alpha q}{1 + \beta q^2} - u \right) \left(-\frac{\alpha q}{(1 + \beta q^2)^2} \right) q^2 \right] = 0 \quad (14)$$

$$\alpha E \left(\frac{q^4}{(1 + \beta q^2)^3} \right) = E \left(\frac{q^3 u}{(1 + \beta q^2)^2} \right) \quad (15)$$

Let's define the following for the sake of simplicity.

$$A(\beta) = E \left(\frac{q^2}{(1 + \beta q^2)^2} \right) \quad (16)$$

$$B(\beta) = E \left(\frac{qu}{1 + \beta q^2} \right) \quad (17)$$

$$C(\beta) = E \left(\frac{q^4}{(1 + \beta q^2)^3} \right) \quad (18)$$

$$D(\beta) = E \left(\frac{q^3 u}{(1 + \beta q^2)^2} \right) \quad (19)$$

According to (13), (16) and (17)

$$\alpha = \frac{B(\beta)}{A(\beta)} \quad (20)$$

and according to (15), (18), (19), (20)

$$\frac{B(\beta)}{A(\beta)} C(\beta) = D(\beta) \quad (21)$$

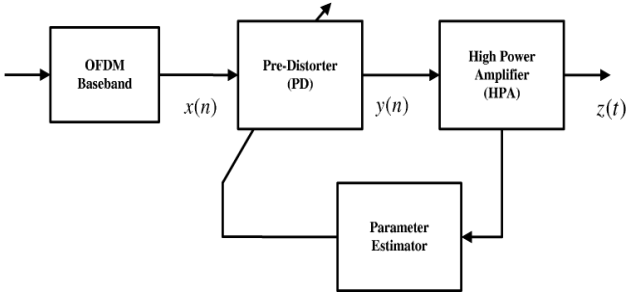


Fig. 4. Block diagram of PD for Time varying HPA

So, the algorithm is: Solve (21) numerically for $\hat{\beta}$, the estimate of β , then replace $\hat{\beta}$ in (20) to obtain $\hat{\alpha}$, the estimate of α . The expectation in (16), (17), (18), (19) can be expressed using following equations

$$A(\beta) = \frac{1}{N} \sum_{n=1}^N \frac{q_n^2}{(1 + \beta q_n^2)^2} \quad (22)$$

$$B(\beta) = \frac{1}{N} \sum_{n=1}^N \frac{q_n u_n}{1 + \beta q_n^2} \quad (23)$$

$$C(\beta) = \frac{1}{N} \sum_{n=1}^N \frac{q_n^4}{(1 + \beta q_n^2)^3} \quad (24)$$

$$D(\beta) = \frac{1}{N} \sum_{n=1}^N \frac{q_n^3 u_n}{(1 + \beta q_n^2)^2} \quad (25)$$

γ and ε also can be estimated exactly same way as described above.

IV. SIMULATION RESULTS AND DISCUSSION

In this section, the validity of proposed predistortion technique for compensation of TWTA nonlinear distortion is demonstrated with computer simulation and presents some discussion about the results. The Additive White Gaussian Noise (AWGN) channels were assumed to clearly observe the effect of nonlinearity and performance improvement by the proposed PD. An OFDM system with 128 subcarrier and 16 QAM is considered. If input amplitude is very high, the HPA operates with highly nonlinear situation. If input amplitude is very small, the HPA operates in very small distortion. In the operation of HPA, relative level of power back off is needed to reduce distortion. However, this power back off is not so desirable. Because, it reduces power efficiency. In our algorithm, compensation solution always exists in the range $r \leq A_0$, where A_0 is maximum output amplitude. So, if input average power is same as A_0^2 , we get maximum power efficiency, but highly nonlinear. Thus, we need a criteria to show how much power back off from optimum power

efficiency. In the simulations, we define IBO (Input Back-Off) as

$$IBO = 10 \log_{10} \left(\frac{A_0^2}{P_{in}} \right) \quad (26)$$

where P_{in} is input average power (average power of baseband OFDM signal). Similarly, we can also define OBO (Output Back-Off) as

$$OBO = 10 \log_{10} \left(\frac{A_0^2}{P_{out}} \right) \quad (27)$$

where P_{out} is output average power (average output power of HPA).

A. OFDM, Time invariant TWTA

In this subsection, we present OFDM simulation results with the assumption that parameters $\alpha, \beta, \gamma, \varepsilon$ are time-invariant. Fig 5. shows the difference of signal constellation with and without PD. In Fig. 5, we use IBO = 6 dB.

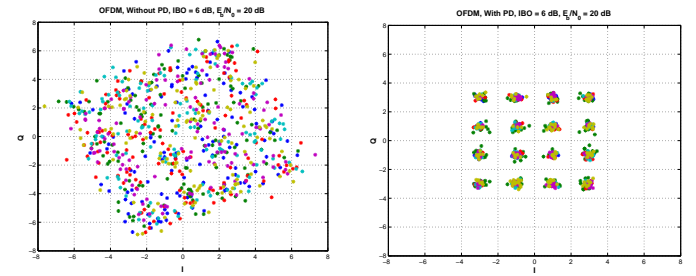


Fig. 5. Received signal constellations of OFDM

The BER performance curve, in Fig. 6, shows that the PD can significantly reduce nonlinear distortion in OFDM system.

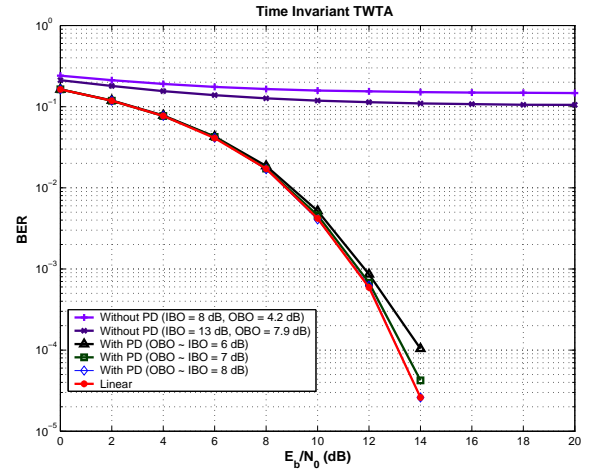


Fig. 6. BER performance of PD in OFDM, with time-invariant HPA

B. OFDM, Time varying TWTA

As we mentioned previously, HPA is time varying system. In this subsection, we assume four parameters $\alpha, \beta, \gamma, \varepsilon$ are time varying, thus we should track the variations of $\alpha, \beta, \gamma, \varepsilon$.

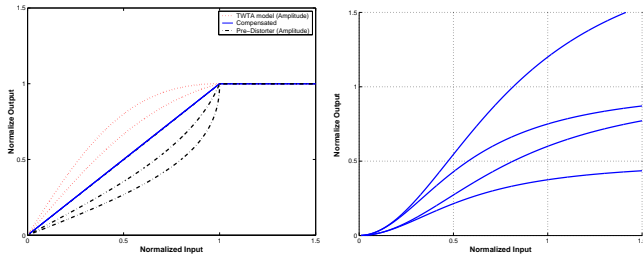


Fig. 7. Some of the examples of amplitude and phase variation

We assume these four parameters change within the following restriction.

(1) Four parameters change in the following ranges

$$1.01 \leq \alpha \leq 2, \quad 0.01 \leq \beta \leq 1, \quad 1.5 \leq \gamma, \varepsilon \leq 3 \quad (28)$$

(2) Input output normalization condition, $\beta = \alpha - 1$.

(3) Saturation condition, signal is clipped above 1, as in Fig 7.

The reason, we choose above restriction in amplitude is to maintain normalization condition in both input and output and saturation condition in the above range, even if the amplitude is changed. These restriction are just for convenience of representation, so, in real system, even if above condition does not hold, our algorithm works well. Table 1 shows errors after tracking $\alpha, \beta, \gamma, \varepsilon$ using our algorithm. We used following equations to get the results of Table 1.

$$\text{Error}(\alpha) = \frac{|\alpha - \hat{\alpha}|}{|\alpha_{max} - \alpha_{min}|}, \quad \text{Error}(\beta) = \frac{|\beta - \hat{\beta}|}{|\beta_{max} - \beta_{min}|}$$

$$\text{Error}(\gamma) = \frac{|\gamma - \hat{\gamma}|}{|\gamma_{max} - \gamma_{min}|}, \quad \text{Error}(\varepsilon) = \frac{|\varepsilon - \hat{\varepsilon}|}{|\varepsilon_{max} - \varepsilon_{min}|}$$

Table 1. Error of parameters

Step size	Error (α)	Error (β)	Error (γ)	Error (ε)
0.1	1.02×10^{-2}	2.74×10^{-2}	6.3×10^{-3}	1.72×10^{-2}
0.01	9.67×10^{-4}	2.5×10^{-3}	6.04×10^{-4}	1.7×10^{-3}
0.001	9.49×10^{-5}	2.54×10^{-4}	6.18×10^{-5}	1.69×10^{-4}

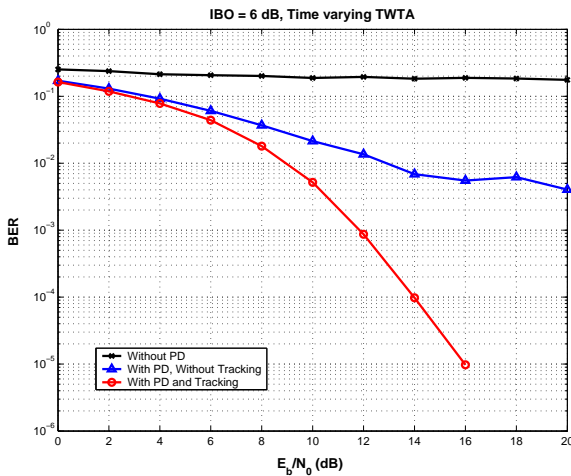


Fig. 8. BER performance of PD in OFDM, with Time varying HPA, IBO = 6 dB

We get the results of Table 1, using only two training sequences, calculating 1000 times and averaging the results. The results of Table 1 shows that only two training sequences are enough for our algorithm. This indicates that our algorithm is very fast and has little delay.

The BER performance of PD in OFDM with time-varying HPA is shown in Fig.8. In this curve, we assume step size = 0.01. As we can see in Fig.8 that if we don't track the variation of HPA, the performance is much worse compared with the case of tracking. The simulation results clearly show that our algorithm works well and is therefore very promising technique.

V. CONCLUSION

We presented a model-based pre-distortion approach for eliminating or mitigating nonlinear distortion in time-varying TWTA amplifier used in OFDM-based wireless communications. The approach uses a closed form inverse of the Saleh model of TWTA, with very few parameters required in the representation of the inverse. This sparse and yet accurate representation enables the tracking the time-varying behavior of the TWTA. These properties have been demonstrated by computer simulations.

REFERENCES

- [1] D. Han and T. Hwang "An adaptive pre-distorter for the compensation of HPA nonlinearity". *IEEE Transactions on Broadcasting*, Vol 1 pp.494-498
- [2] W. G. Jeon, K. H. Chang and Y. S. Cho "An adaptive data predistorter for compensation of nonlinear distortion in OFDM systems". *IEEE Transactions on Communications*, Vol. 45, no 10, pp.1167 - 1171, October 1997
- [3] H. K. Kang, Y. S. Cho, and D. H. Youn "On compensation nonlinear distortions of an OFDM system using an efficient adaptive predistorter". *IEEE Transactions on Communications*, Vol. 47, no 4, pp.522 - 526, April 1999
- [4] S. Chang, E. J. Powers and J. Chung "A compensation scheme for nonlinear distortion in OFDM systems". *Global Telecommunications Conference, 2000. GLOBECOM '00. IEEE*, Vol. 2, pp.736 -740, Dec. 2000
- [5] S. Chang and E. J. Powers, "A simplified predistorter for compensation of nonlinear distortion in OFDM systems". *Global Telecommunications Conference, 2001. GLOBECOM '01. IEEE*, Vol. 5, pp.3080 -3084, Nov. 2001
- [6] Yuanbin Guo, J. R. Cavallaro "Enhanced power efficiency of mobile OFDM radio using predistortion and post-compensation". *IEEE 56th Vehicular Technology Conference, 2002. Proceedings. VTC 2002-Fall. 2002*, Vol. 1, pp. 214 -218, Sept. 2002
- [7] A. A. M. Saleh "Frequency-independent and frequency-dependent nonlinear models of TWT amplifiers" *IEEE Transactions on Communications*, Vol. 29, No. 11, pp.1715 - 1720, Nov. 1981.
- [8] C. Rapp "Effect of HPA-nonlinearity on 4-DPSK/OFDM-signal for a digital sound broadcasting system". *in proceedings of the second European conference on satellite communications*, Liege, Belgium, Oct. 22-24, 1991, pp.179 -184
- [9] A. Brajal and A. Chouly, "Compensation of nonlinear distortions for orthogonal multicarrier schemes using predistortion". *GLOBECOM 1994*, San Francisco, CA, Nov. 1994, vol.3, pp.1909 -1914

NOISE ANALYSIS AND OPTIMIZATION OF GENERAL OTA-C FILTERS

Slawomir Koziel,

*Faculty of Electronics, Telecommunications and Informatics, Gdansk University of Technology, Gdansk, Poland,
koziel@ue.eti.pg.gda.pl*

DOI: 10.36724/2664-066X-2022-8-1-7-12

ABSTRACT

In the paper, a general approach to noise analysis in continuous-time OTA-C filters is presented. Recently an increasing interest in the design of continuous-time filters based on the transconductancecapacitor (OTA-C) technique has been observed. The operational transconductance amplifiers (OTAs) offer a higher bandwidth than their voltage-mode counterparts, can be easily tuned electronically, and have a better suitability for operating in reduced supply environment. Due to this, high frequency integrated filters are mostly realized as the OTA-C ones. Based on a matrix description of a general OTA-C filter topology, a universal formulas for evaluating the noise in any OTA-C filter are derived. The presented formulas can be easily implemented and used in computer-aided analysis/optimization software. The accuracy of the proposed method is confirmed by comparison with SPICE simulation. The example of application for finding the minimum-noise 5th order multiple-loop feedback filters implementing Butterworth and Bessel transfer functions is given.

KEYWORDS: *OTA-C filters, noise analysis, filter optimization.*

The article is reworked from unpublished 2nd IEEE International Conference on Circuits and Systems for Communications (ICCSC) materials.

This work was supported in part by the State Scientific Research Committee, Poland, under Grant 4T11B01625

I. Introduction

Recently an increasing interest in the design of continuous-time filters based on the transconductance-capacitor (OTA-C) technique has been observed [1]-[3]. The operational transconductance amplifiers (OTAs) offer a higher bandwidth than their voltage-mode counterparts, can be easily tuned electronically, and have a better suitability for operating in reduced supply environment [4],[5]. Due to this, high frequency integrated filters are mostly realized as the OTA-C ones [6]. Although these filters offer excellent high frequency performance, their other properties in terms of low supply voltage, low power consumption, low sensitivity, low noise and large dynamic range, etc., still need improvements [5].

In this paper we deal with noise in OTA-C, which limits dynamic range of filters from below. It is important for filter design purposes to develop efficient tools for performing noise analysis of OTA-C filters. There have been several attempts to solve this problem described in the literature [7]-[10]. In this paper we propose a general approach to noise analysis in OTA-C filters based on the matrix description of OTA-C filters developed in [11]. The derived formulas can be applied to any know OTA-C filter architecture. They can also be easily implemented and used in computer-aided analysis/optimization software.

II. General topology of OTA-C filter

Figure 1 shows a general structure of a voltage-mode OTA-C filter. The filter contains n internal nodes denoted as x_i , $i=1,\dots,n$, n input transconductors G_{mbi} , a set of internal feedback and feedforward transconductors G_{mij} , an output summer consisting of transconductors G_{mci} and $-G_{mo}$ as well as a feedforward transconductor G_{md} . All transconductors form active network, while input capacitors C_{bi} , $i=1,\dots,n$ and capacitors C_{ij} , $1 \leq i \leq j \leq n$ form *passive network*. It is easily seen that any OTA-C filter is a particular case of the general structure in Figure 1. A general filter structure in Fig.1 can be described by the following matrix equations [11]:

$$sT_C X = GX + B^T u_i \quad u_o = CX + Du_i \quad (1)$$

where u_i , u_o denote the input and output voltages, respectively, X is a vector of internal node voltages, and

$$\begin{aligned} T_C &= [T_{ij}]_{i,j=1}^n, \quad T_{ii} = C_{bi} + \sum_{j=1}^n C_{ij}, \quad i=1,\dots,n, \\ T_{ij} &= T_{ji} = -C_{ij}, \quad i,j=1,\dots,n, \quad i \neq j \\ G &= [G_{mij}]_{i,j=1}^n, \quad X = [x_1 \quad \dots \quad x_n]^T, \quad D = d = G_{md}/G_{mo} \\ C &= [c_1 \quad \dots \quad c_n], \quad c_i = G_{mci}/G_{mo}, \quad i=1,\dots,n \\ B &= [G_{mb1} + sC_{b1} \quad \dots \quad G_{mbn} + sC_{bn}] \end{aligned} \quad (2)$$

On the basis of (1) we can calculate the filter transfer function:

$$H(s) = \frac{u_o(s)}{u_i(s)} = C(sT_C - G)^{-1} B^T + D \quad (3)$$

Now, let us denote adjoint matrix of $sT_C - G$ as \tilde{A} where

$$\tilde{A}(s) = \text{adj}(sT_C - G) = [\tilde{A}_{ij}(s)]_{i,j=1}^n \quad (4)$$

This allows us to rewrite H in the form:

$$H(s) = [\det(sT_C - G)]^{-1} \sum_{i,j=1}^n c_i (G_{mbj} + sC_{bj}) \tilde{A}_{ij}(s) + d \quad (5)$$

Note that many filter structures have only one input transconductor (i.e. no input signal distribution), a trivial output summer (i.e. one of the internal nodes is the output of the filter), and no input capacitors. This means that $B = [0 \dots 0 \quad G_{mbk} \quad 0 \dots 0]$, $C = [0 \dots 0 \quad 1 \dots 0]$ - 1 at l -th position and $C_{bi} = 0$ for $i=0,1,\dots,n$. Then, (5) reduces to the form of:

$$H(s) = \frac{G_{mbk} \tilde{A}_{lk}(s)}{\det(sT_C - G)} \quad (6)$$

Similar expression can be written for more general cases [11]. On the basis of the above expressions one can easily calculate the transmittance of any structure of OTA-C filter.

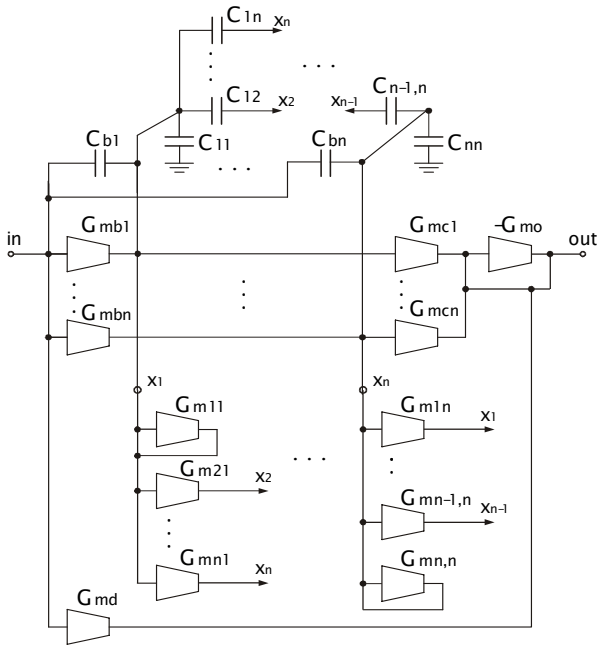


Fig. 1. General structure of voltage-mode OTA-C filter

III. Noise analysis of OTA-C filter

The output noise of any G_m -C filter is a combination of the noise contributions of its all transconductors. The noise in CMOS amplifier with transconductance g_m can be described in terms of an equivalent input referred noise voltage source v_n as shown in Figure 2.

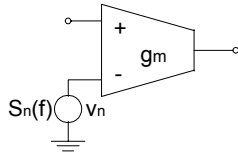


Fig. 2. Input noise source representation of noise in OTA

Spectral density $S_n(f)$ of the noise source can be modeled as [7]:

$$S_n(f) = S_t/g_m + S_f/f \quad (8)$$

where both S_t (thermal noise component) and S_f (flicker noise component) depend on amplifier topology. We shall assume that noise sources associated to different OTAs are statistically independent.

Our immediate goal is to obtain the explicit formula for output (and/or input) noise spectrum of the general OTA-C filter in Fig.1. In order to do this, one has to consider what is the contribution of the noise of each individual transconductance amplifier to the output noise spectrum of the filter. This can be modeled as shown in Fig.3. Let G_{mx} denote one of the filter transconductors (e.g. G_{mbi} , G_{mij} , etc.), which is connected to one of the nodes, say x_i (if the filter contains non-trivial output summer then it has additional output node which will be denoted as x_0). Denote by v_x the input referred noise voltage of the noise source corresponding to G_{mx} , whose spectral density is $S_{vx}(f)$. Transconductor G_{mx} injects its noise current $i_x = v_x G_{mx}$ into the node x_i . Spectral density $S_{ix}(f)$ of this current is given by

$$S_{ix}(f) = G_{mx}^2 S_{vx}(f) \quad (9)$$

The corresponding output noise voltage v_{ox} can be calculated as [7],[8]:

$$v_{ox} = i_x H_i = G_{mx} H_i v_x \quad (10)$$

where H_i is the current-to-voltage transfer function from node x_i to the output of the filter. Corresponding spectral density $S_{vox}(f)$ is given by the formula:

$$S_{vox}(f) = S_{ix}(f) |H_i(j2\pi f)|^2 = G_{mx}^2 S_{vx}(f) |H_i(j2\pi f)|^2 \quad (11)$$

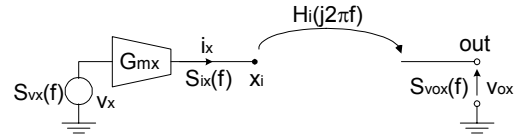


Fig. 3. Noise contribution of individual filter transconductor to the total output noise of the filter

It can be easily shown using the matrix equation (1) that the transfer functions $H_i(s)$, $i=1,2,\dots,n$ are components of the $1 \times n$ vector \mathbf{H}_{cv} defined as follows

$$\mathbf{H}(s) = \mathbf{C}(s\mathbf{T} - \mathbf{G})^{-1} \quad (12)$$

If non-trivial output summer is present (cf. Fig.1) then we need also the current-to-voltage transfer function from output node to itself, which is

$$H_0 = G_{mo}^{-1} \quad (13)$$

Thus, each filter transconductor injects its noise current into one of the internal nodes of the filter (or directly into the output node if the filter possesses nontrivial output summer). Subsequently, this current is converted into output noise voltage according to (11). In order to calculate the total output noise voltage of the filter we add noise spectra due to all transconductors. In general, the outputs of one input transconductor G_{mbi} , and n transconductors G_{mij} , $j=1, \dots, n$ are connected to each internal node x_i . In the presence of non-trivial output summer we have an additional node x_0 with outputs of transconductors G_{mej} , $j=1, \dots, n$, G_{md} , and G_{mo} connected to it. Let us define auxiliary matrices

$$\begin{aligned} \mathbf{S}_t &= [S_{t,ij}]_{i,j=1}^n, \quad \mathbf{S}_f = [S_{f,ij}]_{i,j=1}^n, \\ \mathbf{S}_{tb} &= [S_{tb,1} \quad \dots \quad S_{tb,n}]^T, \quad \mathbf{S}_{fb} = [S_{fb,1} \quad \dots \quad S_{fb,n}]^T, \\ \mathbf{S}_{tc} &= [S_{tc,1} \quad \dots \quad S_{tc,n}], \quad \mathbf{S}_{fc} = [S_{fc,1} \quad \dots \quad S_{fc,n}], \\ \mathbf{S}_{td} &= S_{td}, \quad \mathbf{S}_{fd} = S_{fd}, \quad \mathbf{S}_{to} = S_{to}, \quad \mathbf{S}_{fo} = S_{fo} \end{aligned} \quad (14)$$

representing the thermal noise (subscript t) and $1/f$ noise (subscript f) of transconductors G_{mij} , G_{mbi} , G_{mci} , G_{md} and G_{mo} , respectively. Let us introduce the following notation:

$$\begin{aligned} \mathbf{G} &= [G_{mij}]_{i,j=1}^n, \quad \mathbf{B} = [G_{mb1} \quad \dots \quad G_{mbn}]^T, \\ \overline{\mathbf{C}} &= [G_{mc1} \quad \dots \quad G_{mcn}], \quad \overline{\mathbf{D}} = G_{md}, \quad \overline{\mathbf{O}} = G_{mo} \end{aligned} \quad (15)$$

Denote by \circ the Hadamard product of two matrices, i.e. for $\mathbf{P} = [p_{ij}]_{i,j=1}^n$ and $\mathbf{Q} = [q_{ij}]_{i,j=1}^n$ we have $\mathbf{P} \circ \mathbf{Q} = [p_{ij}q_{ij}]_{i,j=1}^n$ (the same definition holds, with obvious changes for $n \times 1$, $1 \times n$ and 1×1 matrices). Let $\hat{\mathbf{I}} = [1 \quad \dots \quad 1]^T$ be $n \times 1$ vector. Define function $F(\mathbf{P}, \mathbf{Q}, \mathbf{R})(x)$, where \mathbf{P} , \mathbf{Q} , and \mathbf{R} are matrices of the same dimension and x is a real variable:

$$F(\mathbf{P}, \mathbf{Q}, \mathbf{R})(x) = \mathbf{P} \circ (\mathbf{Q} + (2\pi/x)\mathbf{P} \circ \mathbf{R}) \quad (16)$$

It follows from (8) and (9) that spectral densities $S_i(\omega)$ of the total noise current injected into the nodes x_i , $i=1, \dots, n$ can be expressed, using (16), as components of the current spectral density vector \mathbf{S} , given by the formula

$$\begin{aligned} \mathbf{S}(\omega) &= [S_1(\omega) \quad \dots \quad S_n(\omega)]^T = \\ &= F(\overline{\mathbf{G}}, \mathbf{S}_t, \mathbf{S}_f)(\omega) \cdot \hat{\mathbf{I}} + F(\overline{\mathbf{B}}, \mathbf{S}_{tb}, \mathbf{S}_{fb})(\omega) \end{aligned} \quad (17)$$

Spectral density $S_0(\omega)$ of the noise current injected into the node x_0 (if output summer is present) is given by

$$\begin{aligned} S_0(\omega) &= F(\overline{\mathbf{C}}, \mathbf{S}_{tc}, \mathbf{S}_{fc})(\omega) \cdot \hat{\mathbf{I}} + \\ &+ F(\overline{\mathbf{D}}, \mathbf{S}_{td}, \mathbf{S}_{fd})(\omega) + F(\overline{\mathbf{O}}, \mathbf{S}_{to}, \mathbf{S}_{fo})(\omega) \end{aligned} \quad (18)$$

The spectrum density $S_{no}(\omega)$ of the total output noise voltage u_{no} can be then calculated as

$$S_{no}(\omega) = |\mathbf{H}_{cv}(\omega)|^2 \mathbf{S}(\omega) + H_0^2 S_0(\omega) \quad (19)$$

where $|\mathbf{H}_{cv}(\omega)|^2 = \mathbf{H}_{cv}(j\omega) \circ \mathbf{H}_{cv}(-j\omega)$, with \mathbf{H}_{cv} and H_0 given by (12) and (13), respectively. In general, $S_o(\omega)$ is a rational function of ω with numerator and denominator of order not larger than $2n-1$ and $2n+1$, respectively. Formula (19) allows us to calculate the output noise spectrum of any OTA-C filter. In order to get the output noise voltage one needs to integrate (19) over the suitable frequency range. The equivalent input noise spectrum $S_{ni}(\omega)$ can be obtained by dividing (19) by the square of the transfer function of the filter given by (3). It is worth noting that because of matrix formulation, the presented formulas are particularly convenient to be implemented in a computer program which will allow us to carry out the noise analysis of arbitrary OTA-C filter.

In a special case when all transconductors in the filter are the same, each of the matrices \mathbf{S} in (14) is proportional to the unit matrix (i.e. with all entries equal to 1) $\tilde{\mathbf{I}}$ of the suitable dimension, e.g. we have $\mathbf{S}_t = S_t \tilde{\mathbf{I}}$, $\mathbf{S}_f = S_f \tilde{\mathbf{I}}$, where S_t , S_f are noise parameter of transconductor and $\tilde{\mathbf{I}}$ is $n \times n$ unit matrix. Then, equations (17) and (18) take the form

$$\mathbf{S}(\omega) = (\overline{\mathbf{G}}\hat{\mathbf{I}} + \overline{\mathbf{B}})S_t + \frac{2\pi}{\omega} (\overline{\mathbf{G}} \circ \overline{\mathbf{G}}\hat{\mathbf{I}} + \overline{\mathbf{B}} \circ \overline{\mathbf{B}})S_f \quad (20)$$

$$S_0(\omega) = \frac{\overline{\mathbf{C}}}{\hat{\mathbf{I}} + \overline{\mathbf{D}} + \overline{\mathbf{O}}} S_t + \frac{2\pi}{\omega} (\overline{\mathbf{C}} \circ \overline{\mathbf{C}}\hat{\mathbf{I}} + \overline{\mathbf{D}} \circ \overline{\mathbf{D}} + \overline{\mathbf{O}} \circ \overline{\mathbf{O}}) S_f \quad (21)$$

IV. Verification and application example

In this section we discuss an application example of the OTA-C filter noise analysis presented in Section III. Due to its generality and matrix formulation, the presented approach can be used to solve many optimization tasks such as proper choice of filter topology with respect to optimal noise performance or direct optimization of filter noise performance in various settings.

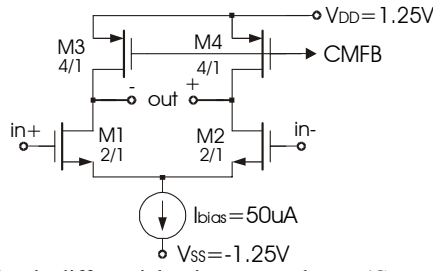


Fig.5. Simple differential-pair transconductor (Common-Mode Feedback circuit not shown)

We start from a verification of the presented approach by comparing the theoretical results of Section III to the SPICE simulation. For our comparison we use a simple differential-pair transconductor shown in Fig.5. The circuit was implemented in standard 0.35 μ m AMS technology. The OTA noise parameters (see (8)) extracted from the simulations are $S_f=5.2 \cdot 10^{-16}$ V \cdot A/Hz, and $S_f=2.3 \cdot 10^{-10}$ V 2 . Transconductance of the circuit equals $g_m=100\mu$ A/V.

The OTA circuit in Fig.5 was used to implement two Butterworth low-pass filters in a leap-frog (LF) structure: third- and eight-order ones. Fig.6 shows a general structure of n^{th} order LF structure. Actual filters were implemented in fully differential structures. 3dB frequency of the filters is 10MHz. Figs.7 and 8 show input and output noise spectrum versus frequency for 3 $^{\text{rd}}$ order and 8 $^{\text{th}}$ order filter respectively. The agreement between theoretical results (line) and SPICE simulation results (point) is very good. The little discrepancy for output noise spectrum in Fig.8 follows not from the limited accuracy of the model but from the fact of finite DC gain of the OTA (in this case about 35dB) which gives DC gain of the filter equal to -1.3dB (instead of ideal value of 0dB)

As an example of noise optimization we shall consider the optimal choice of the multiple-loop feedback topology for the fifth-order low-pass filter. Fig.9 shows the general structure of n -th order all-pole canonical low-pass G_m -C filter. The feedback signal at node x_i can be taken from node x_{k_j} , where $k_j \in \{i+1, \dots, n\}$ for $i < n$, and $k_n = n$. Two most popular multiple-loop feedback topologies - leap-frog (LF) and inverse follow-the-leader (IFLF) can be considered as two 'extreme' canonical structures of all-pole filters [11]. In particular, for LF structure the feedback signal at node x_i is taken from the node x_{i+1} , $i=1, 2, \dots, n-1$ and the node x_n has the inner feedback loop. In IFLF structure all feedback signals at nodes x_i , $i=1, 2, \dots, n$ are taken from the node x_n . In general, the feedback signal emerging at node x_i can be taken from node x_j , where $j=i+1, \dots, n$. Thus, we have in total $(n-1)!$ multiple-loop feedback structures of order n . The matrix approach proposed in Section III makes it possible to perform an exhaustive search through all topologies since it is very fast and can be easily automated.

To simplify further description, we introduce the following notation: let $F_{n|j_1, j_2, \dots, j_n}$ denote the canonical all-pole low-pass structure of n -th order, for which the feedback signal emerging at node x_i is taken from node x_{j_i} . For example, n -th order LF structure will be denoted

as $F_{n|2,3,4, \dots, n, n}$, while n -th order IFLF structure as $F_{n|n, n, \dots, n}$.

Here, we will consider 5 $^{\text{th}}$ order Butterworth and Bessel filters. According to the discussion above, there are 24 different canonical structures that realize this transfer function. They are implemented with the same value of transconductance (equal to 100 μ A/V) for all filter transconductors. Table 1 shows integrated input noise for all the structures and both approximations. The noise is integrated over 3dB bandwidth and normalized to the noise of LF filter. Only thermal noise has been considered in this example. It follows from the results in Table 1 that the difference of integrated noise between best and worst topology is as large as 7dB for Butterworth filters and 4.3dB for Bessel filters. This difference tells us about the improvement in noise performance we can get by proper choice of the filter topology.

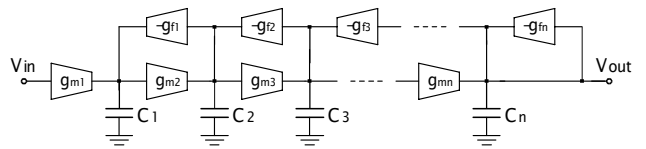


Fig.6. Diagram of n^{th} order LF filter

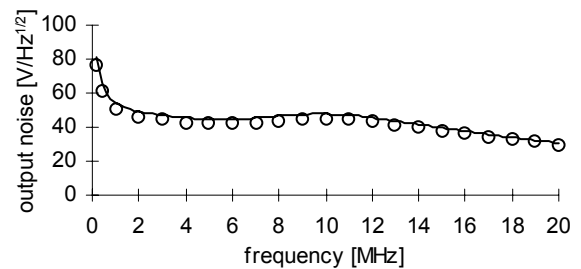
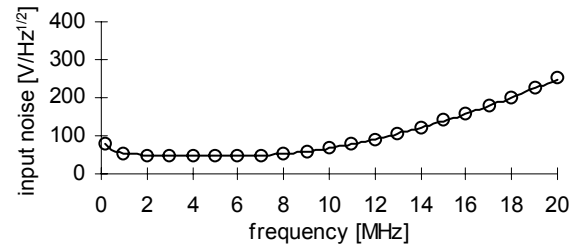


Fig.7. Input and output noise spectrum vs. frequency for 3 $^{\text{rd}}$ order Butterworth filter; theory (line) and simulation (points)

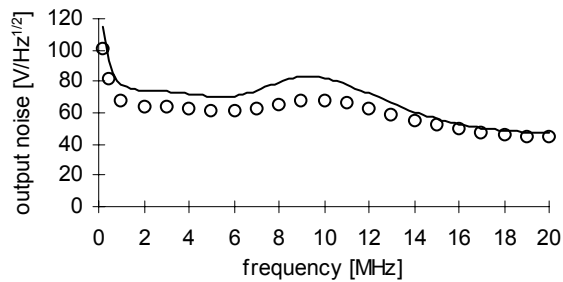
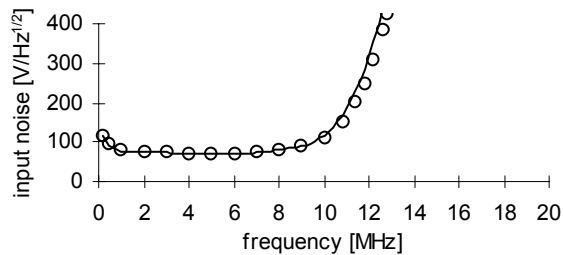


Fig. 8. Input and output noise spectrum vs. frequency for 8th order Butterworth filter; theory (line) and simulation (points)

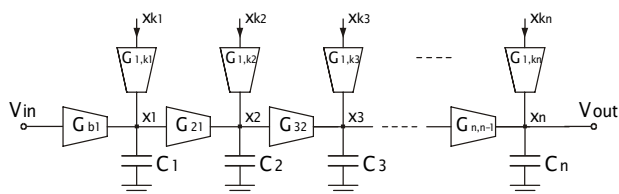


Fig. 9. A general structure of an n -th order all-pole canonical low-pass OTA-C filter

Table 1. Integrated input noise comparison for 5th order all-pole low-pass Butterworth and Bessel filters; best and worst topologies denoted by * and #, respectively

Filter structure	Normalized noise [dB]		Filter structure	Normalized noise [dB]	
	Butterworth	Bessel		Butterworth	Bessel
$F_{5 2,3,4,5,5}$	0.0	0.0	$F_{5 4,3,4,5,5}$	2.6	1.1
$F_{5 2,3,5,5,5}$	-0.2*	-0.4	$F_{5 4,3,5,5,5}$	3.2	1.3
$F_{5 2,4,4,5,5}$	2.4	0.4	$F_{5 4,4,4,5,5}$	5.7	2.4
$F_{5 2,4,5,5,5}$	2.9	-0.1	$F_{5 4,4,5,5,5}$	7.1	3.0
$F_{5 2,5,4,5,5}$	2.4	-0.5	$F_{5 4,5,4,5,5}$	5.3	1.3
$F_{5 2,5,5,5,5}$	3.0	-1.2*	$F_{5 4,5,5,5,5}$	6.8#	2.1
$F_{5 3,3,4,5,5}$	3.4	1.8	$F_{5 5,3,4,5,5}$	3.6	1.9
$F_{5 3,3,5,5,5}$	3.1	1.2	$F_{5 5,3,5,5,5}$	2.9	1.0
$F_{5 3,4,4,5,5}$	6.0	3.1#	$F_{5 5,4,4,5,5}$	6.2	2.9
$F_{5 3,4,5,5,5}$	6.7	2.8	$F_{5 5,4,5,5,5}$	6.7	2.5
$F_{5 3,5,4,5,5}$	5.5	2.1	$F_{5 5,5,4,5,5}$	5.9	1.9
$F_{5 3,5,5,5,5}$	6.2	1.7	$F_{5 5,5,5,5,5}$	6.3	1.3

V. Conclusions

In the paper, an efficient procedure for evaluating noise in general OTA-C filter has been proposed. It has been verified by comparing with SPICE simulation proving its accuracy. The derived formulas can be applied to any know OTA-C filter architecture and can be easily implemented and used in computer-aided analysis/optimization software.

References

- [1] R. Schaumann, M. S. Ghauri, and K. R. Laker, *Design of Analog Filters, Passive, Active RC, and Switched Capacitor*. Englewood Cliff, NJ: Prentice-Hall, 1990.
- [2] T. Deliyannis, Y. Sun, and J. K. Fidler, *Continuous-time active filter design*, CRC Press, USA, 1999.
- [3] R. L. Geiger and E. Sánchez-Sinencio, „Active filter design using operational transconductance amplifiers: A tutorial,” *IEEE Circuit and Devices Mag.*, vol.1, pp.20-32, 1985.
- [4] B. Nauta, *Analog CMOS filters for very high frequencies*, Kluwer Academic Publishers, 1993.
- [5] Y. Sun (Editor), *Design of high frequency integrated analogue filters*, The Institution of Electrical Engineers, London, 2002.
- [6] Y.P. Tsvividis, „Integrated continuous-time filter design - an overview”, *IEEE J. Solid-State Circuits*, vol.29, pp.166-176, 1994
- [7] A. Brambilla, G. Espinosa, F. Montecchi, E. Sánchez-Sinencio, „Noise optimization in operational transconductance amplifier filters,” in *Proc. Int. Symp. Circuits Syst. ISCAS*, Vol.1, pp. 118 -121, 1989.
- [8] G. Ejthivoulidis, L. Toth, Y.P. Tsvividis, „Noise in Gm-C Filters”, *IEEE Trans. Circuits Syst.*, Vol.45, No.3, pp.295-302, Mar. 1998.
- [9] S. Koziel, S. Szczepanski, „Dynamic Range Comparison of Voltage-Mode and Current-Mode State-Space G_m-C Biquad Filters in Reciprocal Structures”, *IEEE Trans. Circuits Syst.-I*, Vol.50, No.10, pp.1245 -1255, Oct.2003.
- [10] Y. Palaskas, Y. Tsvividis, „Dynamic Range Optimization of Weakly Nonlinear, Fully Balanced, Gm-C Filters With Power Dissipation Constraints”, *IEEE Trans. Circuits Syst.-II*, Vol.50, No.10, pp.714-727, Oct.2003.
- [11] S. Koziel, S. Szczepanski, R. Schaumann, „General Approach to Continuous-Time G_m-C Filters”, *Int. J. Circuit Theory Appl.*, Vol.31, pp.361-383, July/Aug. 2003.

ORGANIZERS:

INSTITUTE OF ELECTRICAL AND ELECTRONICS ENGINEERS (IEEE)
IRIS ASSOCIATION (INSTITUTE OF RADIO AND INFORMATION SYSTEMS, VIENNA, AUSTRIA)
RUSSIA SECTION TEM/GRS/ITSS JOINT CHAPTER

INTERNATIONAL CONFERENCE

**«2022 International Conference
«Engineering Management of
Communication and Technology»
(EMCTECH)**

IEEE Conference #55220

**20 – 22 October 2022
Vienna, Austria**

Conference will produce a publication.

All accepted and presented Papers following the conference will be submitted for inclusion into IEEE Xplore and will be submitted also for indexing in Scopus and Web of Science data bases

The papers which are discussed at the conference can be divided into the following chapters:

CHAPTER 1. TECHNOLOGY ADVANCEMENTS IN IOT DEVICES

CHAPTER 2. TECHNOLOGY ADVANCEMENTS IN ARTIFICIAL INTELLIGENCE

Subsection 2.1. Philosophy of Artificial Intelligence – Man in Intelligent Communication Systems

CHAPTER 3. TRANSPORT AND COLLECTIVE SYSTEMS: SMART CONTROL TECHNOLOGY IN TRANSPORTATION, BIOMEDICAL, FARMING AND CYBER PHYSICAL SYSTEMS (new opportunities using technology in biomedical, farming, transportation, and cyber physical systems)

Subsection 3.1. Technology advancements in creating sustainable engines

Subsection 3.2. Smart Highway Maintenance: Advanced Technology of Control and Design

CHAPTER 4. BROADCAST TECHNOLOGIES ADVANCEMENTS – RADIO, IP, CELLULAR, ON DEMAND, INTERACTIVE

CHAPTER 5. TECHNOLOGY ADVANCEMENTS IN WIRE AND OPTICAL COMMUNICATION AND CONTROL SYSTEMS

CHAPTER 6. DIGITALIZATION PROCESS AND SECURITY MANAGEMENT IN DIGITAL SOCIETY AND INDUSTRY 4.0

CHAPTER 7. DIGITAL TRANSFORMATION AND DATA RISK MANAGEMENT IN ICT/TELECOMMUNICATION

CHAPTER 8. DEVELOPING PERSONAL SKILLS FOR LEADING INNOVATION INITIATIVES

CHAPTER 9. ENGINEERING TECHNOLOGY LEADING TO SOCIAL AND ECONOMICAL CHANGE

Submission dates

Full Paper Submission date: 15 August 2022

Notification of Acceptance date: 30 August 2022

Materials are available in English

<http://media-publisher.eu/conference-emctech/call-for-papers/>

NONIDEAL BEHAVIOUR OF OA-BASED ASTABLE MULTIVIBRATORS WITH APPLICATIONS IN LINEAR CAPACITANCE- AND INDUCTANCE-TO-TIME CONVERSIONS

*Romeo Ghinea, Liviu Goras, Tecla Goras,
TUIASI, Iasi, Romania
rghinea@etc.tuiasi.ro*

*Michael Ansorge,
University of Neuchatel (UniNE), Neuchatel, Switzerland*

DOI: 10.36724/2664-066X-2022-8-1-14-19

ABSTRACT

The nonideal behaviour of astable multivibrators based on Negative Impedance Converter (NIC) type configuration is approached taking into consideration several nonidealities among which the slew-rate of the voltage operational amplifier (OA). Linear conversion of inductances, capacitances and resistances into time period is useful to measure impedances or physical quantities by means of impedance-type transducers. Following a series of investigations on this topic, a thorough study of four configurations for linear inductance-time and capacitance-time conversions based on the astable multivibrator viewed as a NIC-type nonlinear oscillator. Four circuits were studied, two of them having grounded reactive elements. The results can be used for linear capacitance-to-time (C|T) and inductance-to-time (L|T) conversions.

KEYWORDS: *Negative Impedance Converter, operational amplifier, capacitance-to-time, inductance-to-time.*

The article is reworked from unpublished 2nd IEEE International Conference on Circuits and Systems for Communications (ICCSC) materials.

I. Introduction

Linear conversion of inductances, capacitances and resistances into time period is useful to measure impedances or physical quantities by means of impedance-type transducers. Following a series of investigations on this topic [2–4], a thorough study of four configurations for linear inductance-time and capacitance-time conversions based on the astable multivibrator viewed as a NIC-type nonlinear oscillator has been reported in [5]. The L|T converter proposed in [2] consisted of a single OA astable multivibrator having the capacitor simulated by a two OA gyrator loaded by the inductance to be measured. The much simpler technique presented in [3] consisted of a single OA astable multivibrator, three resistances and the (ungrounded) inductance to be measured. To eliminate the disadvantage of the ungrounded inductance, a two OA-s L|T converter was proposed in [4]. In [5], the general theory of multivibrators viewed as NIC-type configurations, and the formulae for the time period taking into consideration the losses of the reactive elements were presented. The theory was based on the fact that the simplest astable multivibrators consist of a parallel connection of an inductor (capacitor) and an N-type (S-type) resistance. The possibilities to obtain N- and S-type negative resistances using one OA-based NIC configuration by taking into consideration the OA output saturation resistances (which strongly influence the shape of the voltage-current characteristics (u, i)) and thus the period of oscillation) have been studied. In this way, a systematic study of a single OA family of L|T and C|T converters has been performed, resulting in a new L|T converter which was not only very simple, but exhibited also the advantage of a grounded inductance. Later, in [6], it has been shown for one of the L|T converters derived in [5], that for small time periods, when the slew rates strongly affect the circuit behavior, the L|T conversion is linear as well.

The aim of this paper is to present several improved results regarding all four types of single OA-based astable multivibrators using NIC-type configurations, when running in those regimes where the OA slew rates strongly affect their behavior. Using a time-domain analysis, it will be shown that the C|T and L|T conversions are linear, irrespective of the fact that the reactive element is grounded or not.

II. Basic Circuit

All results refer to the general configuration shown in Fig.1 where the passive elements including the parasitic resistances (R_p) are specified as indicated in Tab.1. When the oscillation conditions are satisfied and the operating frequency is low, the OA output behaves roughly like a piece-wise constant voltage source, switching between positive and negative polarity. However, when the operating frequency is sufficiently high, the OA output behaves as a voltage source v_s generating a triangular waveform (due to slew rate limitations) in series with an output resistance R_{OUT} .

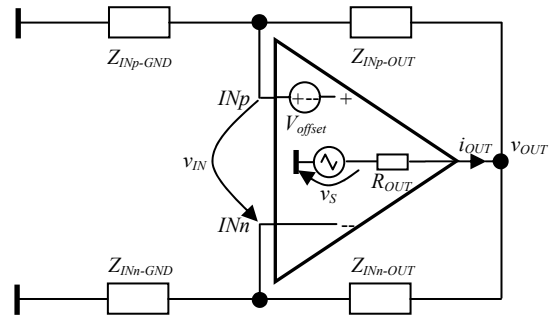


Fig.1 General schematic of a NIC-type astable multivibrator

Tab.1	C-type astable multivibrators		L-type astable multivibrators	
	C grounded	C floating	L grounded	L floating
$Z_{INp-GND}$	R_1	R_0	Series(L_0, R_p)	R_2
$Z_{INp-OUT}$	R_2	Parallel(C_0, R_p)	R_0	R_1
$Z_{INn-GND}$	Parallel(C_0, R_p)	R_2	R_1	R_0
$Z_{INn-OUT}$	R_0	R_1	R_2	Series(L_0, R_p)

In the following, the astable multivibrators based on the configuration depicted in Fig.1 will be studied under the hypothesis that the oscillation period is sufficiently low so that the OA output voltage v_{OUT} (current i_{OUT}) is below the saturation (limitation) values and v_s source exhibits a triangular waveform with slopes equal to the slew rates. Denoting by V_{min} and V_{max} the minimum and maximum values of the triangularly shaped voltage v_s , and by SR_p and SR_n its positive and negative slopes determined by the slew rates, then the rise and fall times are respectively $t_r = (V_{max} - V_{min})/SR_p$ and $t_f = (V_{min} - V_{max})/SR_n$, corresponding to

an oscillation period of $T = t_r + t_f$. Using over the elementary oscillation period the following waveform for the voltage source

$$v_s(t) = v_{S(r)}(t)(\sigma(t) - \sigma(t - t_r)) + v_{S(f)}(t - t_r)(\sigma(t - t_r) - \sigma(t - t_r - t_f))$$

where $v_{S(r)}(t) = V_{\min} + SR_p t$ and $v_{S(f)}(t) = V_{\max} - SR_n t$ are the rising and falling components, respectively, and $\sigma(t)$ denotes the Heaviside function, the OA input voltage,

$v_{IN}(t)$, can be easily found in closed form, since the external network is linear. Once the input differential voltage $v_{IN}(t)$ is found, two sets of conditions can be used to determine the oscillation period:

- Crossing zero value conditions (**ZC**):

$$\begin{cases} v_{IN}(0) - V_{offset} = 0 \\ v_{IN}(t_r) - V_{offset} = 0 \end{cases} \text{ or equivalently } \begin{cases} v_{IN}(t_r) - V_{offset} = 0 \\ v_{IN}(t_r + t_f) - V_{offset} = 0 \end{cases}$$

- Piecewise constant polarity conditions (**PC**):

$$\begin{cases} v_{IN}(t) - V_{offset} > 0, t \in (0, t_r) \\ v_{IN}(t) - V_{offset} < 0, t \in (t_r, t_r + t_f) \end{cases}$$

In the conditions above, V_{offset} denotes the OA input offset voltage, cf. Figure 1.

III. Input differential voltage and oscillation period

The linear network transfer functions from the output to the differential input of the OA, $H_{IN}(s) = V_{IN}(s)/V_S(s)$, has the form $H_{IN}(s) = k(s - \alpha)/(s + \beta)$, where $\alpha = 1/(R_\alpha C_0)$, $\beta = 1/(R_\beta C_0)$ or $\alpha = R_\alpha/L_0$, $\beta = R_\beta/L_0$, according to the type of reactive element used, while k and R_α , R_β are given in Tab.2. Applying Tab.1, we observe that the transfer function $H_{IN}(s)$ has the same form for any C- and L-type astable multivibrator, irrespective of the fact that the reactive element is grounded or not.

Tab.2	C-type astable multivibrator (grounded or floating)	L-type astable multivibrator (grounded or floating)
k	$\frac{1}{\left(1 + \frac{R_2}{R_1}\right) \left \frac{R_f}{R_0} \right + \frac{R_f}{R_0}} \frac{1}{4} \frac{R_{OUT}}{R_1}$	$\frac{1}{1 + \frac{1 + R_{OUT} R}{R_2}}$
R_α	$\frac{1}{\frac{R_2}{R_0 R_1} - \frac{1}{R_p}}$	$\frac{R_0 R_1}{R^2} - p$
R_β	$\frac{1}{\frac{1}{R_p} + \frac{1}{R_0 + \frac{1}{\frac{1}{R_{OUT}} + \frac{1}{R_1 + \frac{1}{R}}}}}$	$R_p + \frac{R_0}{\frac{1}{R_{OUT}} + \frac{1}{R_1 + \frac{1}{R}}}$

The waveform of the OA input differential voltage for an oscillation period has the analytical expression:

$$v_{IN}(t) = v_{IN(r)}(t)(\sigma(t) - \sigma(t - t_r)) + v_{IN(f)}(t - t_r)(\sigma(t - t_r) - \sigma(t - t_r - t_f))$$

where the two components corresponding to the voltage source rise and fall time intervals are respectively:

$$\begin{aligned} v_{IN(r)}(t) &= k \left(\frac{SR_p}{\beta} \left(1 + \frac{\alpha}{\beta} \right) - V_{\min} \frac{\alpha}{\beta} \right) - k \frac{\alpha}{\beta} SR_p t - \\ & k \left(1 + \frac{\alpha}{\beta} \right) \frac{SR_p - SR_n}{\beta} \frac{e^{\beta t_r} (e^{\beta t_r} - 1)}{(e^{\beta(t_r + t_f)} - 1)} e^{-\beta t} \\ v_{IN(f)}(t) &= k \left(\frac{SR_n}{\beta} \left(1 + \frac{\alpha}{\beta} \right) - V_{\max} \frac{\alpha}{\beta} \right) - k \frac{\alpha}{\beta} SR_n t - \\ & k \left(1 + \frac{\alpha}{\beta} \right) \frac{SR_n - SR_p}{\beta} \frac{e^{\beta t_f} (e^{\beta t_f} - 1)}{(e^{\beta(t_r + t_f)} - 1)} e^{-\beta t} \end{aligned}$$

The (**ZC**) and (**PC**) conditions can be expressed as:

$$\begin{cases} v_{IN(r)}(0) - V_{offset} = 0 \\ v_{IN(f)}(0) - V_{offset} = 0 \end{cases} \text{ and } \begin{cases} v_{IN(r)}(t) - V_{offset} > 0, t \in (0, t_r) \\ v_{IN(f)}(t) - V_{offset} < 0, t \in (0, t_f) \end{cases}$$

When (**ZC**) conditions are used the following, two equations in V_{\min} and V_{\max} are obtained:

$$\begin{aligned} V_{\min} &= -V_{offset} \frac{\beta}{k\alpha} + \\ & \left(\frac{1}{\alpha} + \frac{1}{\beta} \right) \frac{SR_p \left(\coth \left(\frac{1}{2} \frac{V_{\min} - V_{\max}}{SR_n / \beta} \right) - 1 \right) + SR_n \left(\coth \left(\frac{1}{2} \frac{V_{\max} - V_{\min}}{SR_p / \beta} \right) + 1 \right)}{\coth \left(\frac{1}{2} \frac{V_{\min} - V_{\max}}{SR_n / \beta} \right) + \coth \left(\frac{1}{2} \frac{V_{\max} - V_{\min}}{SR_p / \beta} \right)}, \\ V_{\max} &= -V_{offset} \frac{\beta}{k\alpha} + \\ & \left(\frac{1}{\alpha} + \frac{1}{\beta} \right) \frac{SR_n \left(\coth \left(\frac{1}{2} \frac{V_{\max} - V_{\min}}{SR_p / \beta} \right) - 1 \right) + SR_p \left(\coth \left(\frac{1}{2} \frac{V_{\min} - V_{\max}}{SR_n / \beta} \right) + 1 \right)}{\coth \left(\frac{1}{2} \frac{V_{\max} - V_{\min}}{SR_p / \beta} \right) + \coth \left(\frac{1}{2} \frac{V_{\min} - V_{\max}}{SR_n / \beta} \right)}, \end{aligned}$$

which lead to the equation below for the voltage source peak-to-peak value ($V_{\max} - V_{\min}$) of the voltage source v_s :

$$\frac{1}{2} \frac{V_{\max} - V_{\min}}{SR_p - SR_n} \left(\coth \left(\frac{1}{2} \frac{V_{\max} - V_{\min}}{SR_p / \beta} \right) - \coth \left(\frac{1}{2} \frac{V_{\max} - V_{\min}}{SR_n / \beta} \right) \right) = \frac{\alpha}{\beta} + \frac{1}{\beta}$$

Since the oscillation period is related to the voltage source peak-to-peak value through the relationship $T = (V_{\max} - V_{\min}) / (1/SR_p - 1/SR_n)$, the next equation can be derived for the oscillation period, T :

$$\frac{\beta T}{2K_{SR}} \left(\coth \left(\frac{\beta T}{4} \left(1 - \sqrt{1 - \frac{4}{K_{SR}}} \right) \right) + \coth \left(\frac{\beta T}{4} \left(1 + \sqrt{1 - \frac{4}{K_{SR}}} \right) \right) \right) = 1 + \frac{\beta}{\alpha}$$

where $K_{SR} = -SR_p/SR_n - SR_n/SR_p$ may be interpreted as a measure of the slew rate relative error, since $K_{SR} \geq 4$ (the equality is valid if $SR_p = -SR_n$).

Capacitor based astable multivibrators

For $\alpha = 1/(R_\alpha C_0)$ and $\beta = 1/(R_\beta C_0)$, the oscillation period is specified by $T = R_x C_0$, where R_x is the positive solution of the transcendental equation:

$$\frac{R_x}{2K_{SR}R_\beta} \left(\coth \left(\frac{R_x}{4R_\beta} \left(1 - \sqrt{1 - \frac{4}{K_{SR}}} \right) \right) + \coth \left(\frac{R_x}{4R_\beta} \left(1 + \sqrt{1 - \frac{4}{K_{SR}}} \right) \right) \right) = 1 + \frac{R_\alpha}{R_\beta}$$

The parameters V_{\min} and V_{\max} become respectively:

$$V_{\min} = -V_{\text{offset}} \frac{R_\alpha}{kR_\beta} + \frac{1}{2} \frac{R_x C_0}{K_{SR}} \left(SR_p \left(\coth \left(\frac{R_x}{1 - SR_n/SR_p} \right) - 1 \right) + SR_n \left(\coth \left(\frac{R_x}{1 - SR_p/SR_n} \right) + 1 \right) \right)$$

$$V_{\max} = -V_{\text{offset}} \frac{R_\alpha}{kR_\beta} + \frac{1}{2} \frac{R_x C_0}{K_{SR}} \left(SR_n \left(\coth \left(\frac{R_x}{1 - SR_p/SR_n} \right) - 1 \right) + SR_p \left(\coth \left(\frac{R_x}{1 - SR_n/SR_p} \right) + 1 \right) \right)$$

Inductor based astable multivibrators

For $\alpha = R_\alpha/L_0$ and $\beta = R_\beta/L_0$, the oscillation period is determined by $T = L_0/R_x$, where R_x is the positive solution

$$\frac{R_\beta}{2K_{SR}R_x} \left(\coth \left(\frac{R_\beta}{4R_x} \left(1 - \sqrt{1 - \frac{4}{K_{SR}}} \right) \right) + \coth \left(\frac{R_\beta}{4R_x} \left(1 + \sqrt{1 - \frac{4}{K_{SR}}} \right) \right) \right) = 1 + \frac{R_\beta}{R_\alpha}$$

The parameters V_{\min} and V_{\max} are then given by:

$$V_{\min} = -V_{\text{offset}} \frac{R_\beta}{kR_\alpha} + \frac{1}{2} \frac{L_0}{K_{SR}R_x} \left(SR_p \left(\coth \left(\frac{R_\beta}{1 - SR_n/SR_p} \right) - 1 \right) + SR_n \left(\coth \left(\frac{R_\beta}{1 - SR_p/SR_n} \right) + 1 \right) \right)$$

$$V_{\max} = -V_{\text{offset}} \frac{R_\beta}{kR_\alpha} + \frac{1}{2} \frac{L_0}{K_{SR}R_x} \left(SR_n \left(\coth \left(\frac{R_\beta}{1 - SR_p/SR_n} \right) - 1 \right) + SR_p \left(\coth \left(\frac{R_\beta}{1 - SR_n/SR_p} \right) + 1 \right) \right)$$

Discussion

- 1) From the above relations it can be seen that for each type of astable multivibrator, the oscillation period and the minimum and maximum values of v_s all depend linearly on the capacitance or inductance.
- 2) A necessary and sufficient condition for the existence of a (unique) positive solution of the transcendental equations is $R_\alpha > 0$ (since $R_\beta > 0$ according to Tab.2).

If this condition is satisfied, it is easy to prove that the (PC) conditions are satisfied as well. The above constraint leads to corresponding constraints regarding the loss resistances of the reactive elements:

- For C-type astable multivibrators: $R_p > R_1 R_0 / R_2$
 - For L-type astable multivibrators: $R_p < R_1 R_0 / R_2$.
- 3) The approximation $K_{SR} \approx 4$ can be adopted, since a $\pm 10\%$ deviation of the slew rates around their nominal value leads to an increase of K_{SR} remaining within 1% from its minimal value $K_{SR} = 4$ (usually the slew rates errors are below the specified margins).

In the case $K_{SR} = 4$ (i.e. $SR_p = -SR_n = SR$) gets verified, the above equations become much simpler:

- For C-type astable multivibrators, the value of the resistance R_x is the solution of the equation $R_x \coth(R_x/(4R_\beta))/(4R_\beta) = 1 + R_\alpha/R_\beta$, while $T = R_x C_0$ and $V_{\min, \max} = \mp R_x C_0 SR / 4 - V_{\text{offset}} R_\alpha / kR_\beta$. In the last expression, $V_{\min, \max}$ stands for V_{\min} or V_{\max} , the leading negative or positive sign applying for V_{\min} or V_{\max} , respectively.
- For L-type astable multivibrators, the value of the resistance R_x is the solution of the equation $R_\beta \coth(R_\beta/(4R_x))/(4R_x) = 1 + R_\beta/R_\alpha$, while $T = L_0/R_x$ and $V_{\min, \max} = \mp L_0 SR / (4R_x) - V_{\text{offset}} R_\beta / kR_\alpha$.

It is easily verified that the period depends neither on the slew rate values, nor on the offset voltage, but that it depends only on the OA output resistance and on the passive network elements. Moreover, the minimum and maximum values of v_s depend linearly on the slew rate and input offset voltage values.

- 4) It can be shown that R_x is bounded and can be approximated as follows:

- In the case of C-based astable multivibrators,

$$K_{SR} R_\alpha < R_x < K_{SR} (R_\alpha + R_\beta) \text{ and } R_x \approx R_{xa} = \begin{cases} 2K_{SR} \sqrt{R_\alpha R_\beta}, R_\alpha \leq R_\beta \\ K_{SR} (R_\alpha + R_\beta), R_\alpha \geq R_\beta \end{cases}$$

The maximum of the relative error absolute value $|R_{xa}/R_x - 1|$ is $\sqrt{K_{SR}/3} - 1 = \sqrt{4/3} - 1 < 16\%$ for $R_\alpha \ll R_\beta$, and

decreases fast when R_α/R_β increases, cf. Fig.2-C(b).

- In the case of L-based astable multivibrators,

$$\frac{1/K_{SR}}{1/R_\alpha + 1/R_\beta} < R_x < \frac{R_\alpha}{K_{SR}} \quad \text{and} \quad R_x \approx R_{xa} = \begin{cases} \sqrt{R_\alpha R_\beta}, R_\beta \leq R_\alpha \\ 1/K_{SR}, R_\beta \geq R_\alpha \end{cases}$$

The maximum of the relative error absolute value $|R_{xa}/R_x - 1|$ is $1 - \sqrt{3/K_{SR}} = 1 - \sqrt{3}/4 < 14\%$ for $R_\beta \ll R_\alpha$, and decreases fast when R_β/R_α increases, cf. Fig.2-L(b).

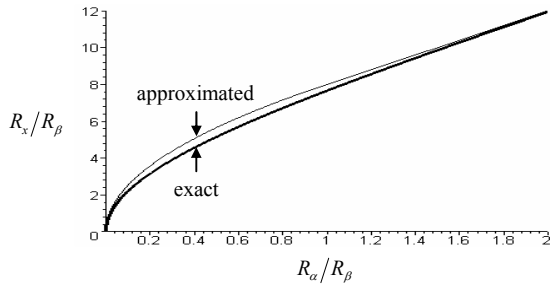


Fig.2-C(a) C-type astable multivibrators – dependence of the approximated (i.e. R_{xa}/R_β) and exact R_x/R_β ratios versus R_α/R_β

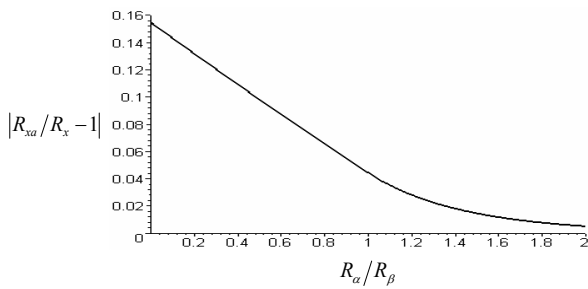


Fig.2-C(b) C-type astable multivibrators – dependence of the relative error absolute value $|R_{xa}/R_x - 1|$ on R_α/R_β

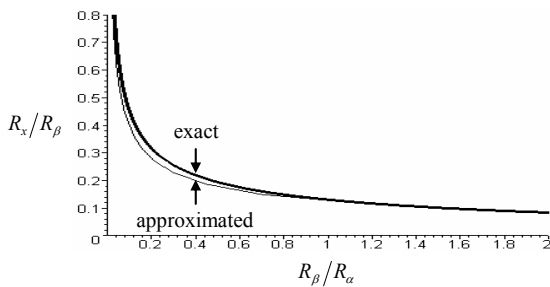


Fig.2-L(a) L-type astable multivibrators - dependence of the approximated (i.e. R_{xa}/R_β) and exact R_x/R_β ratios versus R_β/R_α

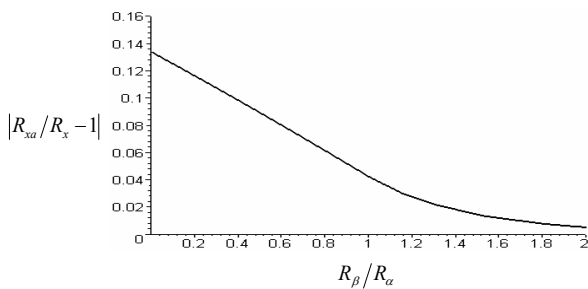


Fig.2-L(b) L-type astable multivibrators - dependence of the relative error absolute value $|R_{xa}/R_x - 1|$ on R_β/R_α

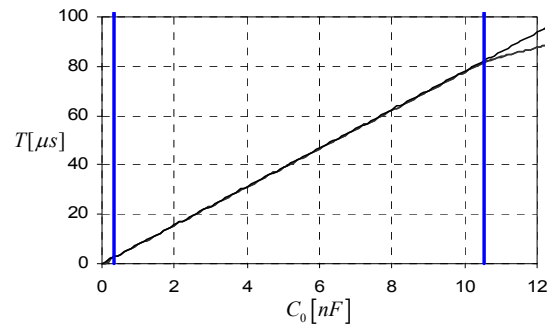


Fig.3-C(a) C-type astable multivibrators – dependence of the oscillation period on the capacitance

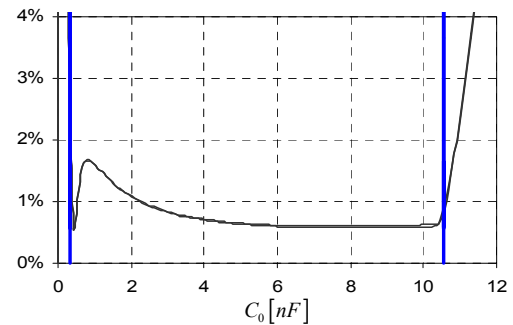


Fig.3-C(b) C-type astable multivibrators – dependence of the absolute value of the oscillation period relative error on the capacitance

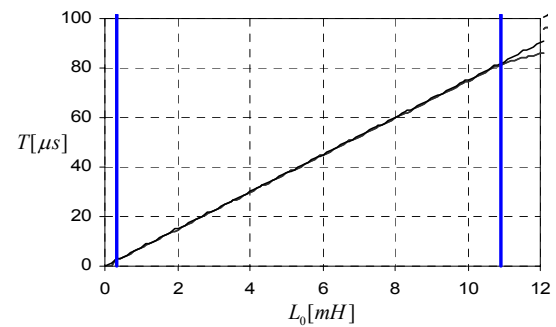


Fig.3-L(a) L-type astable multivibrators – dependence of the oscillation period on the inductance

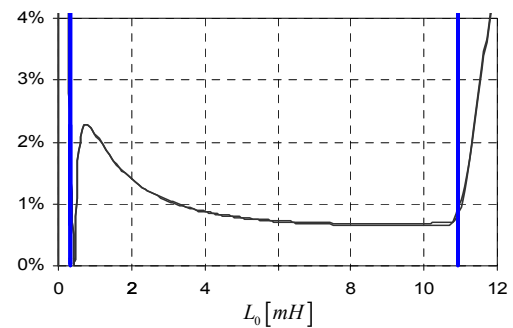


Fig.3-L(b) L-type astable multivibrators – dependence of the absolute value of the oscillation period relative error on the inductance

IV. Simulation results

A large number of parametric transient analyses have been performed using the PSPICE simulator. For the active device (OA), the PSPICE behavioral model of the general purpose LM741 amplifier has been used. Various supply voltages and R_0 , R_1 , R_2 values have been considered to better emphasize the behavior of the circuits. The simulation results match very well the theoretical model. As seen from Fig.3-C(a) and Fig.3-L(a), where the OA-external resistances have identical values ($1K\Omega$) and the OA is symmetrically biased ($\pm 10V$), the simulation results for the cases of grounded and floating reactive elements practically coincide and fit remarkably well to the theoretical behavior represented by the straight lines. This is confirmed by Fig.3-C(b) and Fig.3-L(b) depicting each the relative errors for both grounded and floating reactive element cases, which remain below 2.5% over the entire domain bounded by thick vertical lines within which the OA macro-model used is valid. The relative error abruptly increases for very small capacitance or inductance values for which the circuit approaches the stability limit, as well as for higher values where the OA output stage is working nonlinearly due to voltage saturation or current limitation.

V. Conclusions

Several results regarding OA-based C- and L-type astable multivibrators have been derived considering finite slew-rates and further nonidealities, i.e. OA output resistance and offset voltage, and parasitic resistances of the external reactive elements. The results show that linear C|T and L|T conversions are ensured even under such conditions. The scaling factor between the oscillation period and the value of the reactive element used depends only on the OA-external resistances and on *ratios of slew rates*, irrespective of the fact that the reactive element was grounded or not.

References

- [1]. L. Goraş, C. Mărcuţă, "Nonlinear Synthesis Using Saturation of the Operational Amplifier", *Bulletin of Polytechnic Inst. of Iaşi*, Tom XXVI(XXX), Fasc. 1-2, pp. 25-30, 1980.
- [2]. R. Senani, "A New Technique for Inductance-to-Time Period Conversion Using Integrated Operational Amplifiers", *IEEE Trans. on Industrial Electronics*, Vol. IE-27, No. 1, pp. 36-37, Feb. 1980.
- [3]. L. Goraş, C. Mărcuţă, "Comment on A New Technique for Inductance-to-Time Period Conversion Using Integrated Operational Amplifiers", *IEEE Trans. on Industrial Electronics*, Vol. IE-32, No. 1, pp. 85, Feb. 1985.
- [4]. R. Senani, "On Linear Inductance-Time and Related Conversions Using IC Op Amps", *IEEE Trans. on Industrial Electronics*, Vol. IE-34, No. 2, pp. 292-293, May 1987.
- [5]. L. Goraş, C. Mărcuţă, "On Linear Inductance and Capacitance Time Conversions Using NIC-Type Configurations", *IEEE Trans. on Industrial Electronics*, Vol. 40, No. 5, pp. 529-531, Oct. 1993.
- [6]. L. Goraş, T. Goraş, V. Cehan, R. Ghinea, "On linear time-inductance conversion", *Proc. of 6-th Int'l. Symp. for Design and Technology for Electronic Modules*, Bucharest, Romania, Sept. 2000, pp. 149 - 153.

A PROGRAMMABLE DSP CORE DESIGN FOR SPEECH/AUDIO CODEC SOC

Chin-Teng Lin, Jen-Feng Chung, and Der-Jenq Liu,

*Department of Electrical and Control Engineering, National Chiao-Tung University, Taiwan,
jfchung@falcon3.cn.nctu.edu.tw*

DOI: 10.36724/2664-066X-2022-8-1-20-24

ABSTRACT

A novel programmable DSP core, called LASP24 (Low-cost Application-driven Speech Processor, with 24-bit data width), is developed. It is targeted as a wide-range platform of multimedia applications. The processor core is optimized to efficiently perform fundamental operations for speech/audio signal processing such as vector and matrix operations, and it can be easily embedded into the SOC platform. The design is fabricated with the UMC 0.18 μm standard-cell technology in the total area of 6.5 mm^2 , and it can operate at 100 MHz. It has also been demonstrated that the MELP speech coding and the sound reverberation method could be executed in real-time on the LASP24 operating at 80 Mhz. The assembler and emulator environment have also been developed for designers to verify their algorithms.

KEYWORDS: *MELP, reverberation, vector, matrix, LPC, floating-point, emulator, autocorrelation.*

The article is reworked from unpublished 2nd IEEE International Conference on Circuits and Systems for Communications (ICCSC) materials.

I. Introduction

In recent years, the tremendous progress in VLSI technology allows the integration of an increasing number of transistors on a single chip. The continuous development of multimedia signal processing (DSP) applications makes the algorithms more sophisticated, and they also rely on more computing power for real-time implementation. The trend of consumer electronics is “portable” that means realizing the multimedia processing algorithms on a stand alone low-cost DSP processor [1],[6] within a System-on-Chip (SOC) platform instead of on a high-performance CPU in a PC.

For speech communication, a 2.4 kb/s Mixed Excitation Linear Prediction (MELP) algorithm [2] was standardized in 1997. MELP is similar to classical Linear Prediction Coding (LPC) but with additional features. The new standard provides equal or improved performance over 4.8 kb/s speech coder at only 2.4 kb/s. For audio effect, simulating an acoustic room means finding a system that describes the properties of sound beam propagation from the source of sound towards the listener in an open or closed room. Schroeder [3] implemented the first simulated room algorithm in 1961. Long reverberation times provide the feeling of a large hall, while short reverberation times give the impression of smaller rooms. These two applications can be embedded on the proposed programmable DSP core design.

DSP applications are generally characterized as computationally intensive with a large data set, accumulation-based operations, and loop-dominant control flow behavior. A general-purpose DSP can perform speech or audio processing with high flexibility, but the cost is relatively high. The optimal solution is an application-driven processor core [5], which has a lower cost than a general-purpose processor. In this paper, the implementation of an application-driven processor called LASP24 (Low-cost Application-driven Speech Processor, 24-bit data width) is proposed and it can be integrated into a 32-bit AMBA AHB system bus [4]. The specific addressing modes of LASP24 can quickly execute matrix operations without extra overhead. The advantages of this design include high flexibility in use, small area on silicon, high data throughput, fast portability to a wide range of multimedia technologies, and integrated in the SOC design.

II. System Architecture and Development

Accompanying the rapid development cycles, programmability is a fundamental requirement of a versatile platform designed for the new-generation multimedia applications and standards. The first step of developing a speech/audio codec SOC is to design a programmable DSP core. The proposed system architecture, as shown in Fig. 1, comprises a microcontroller and a programmable core. A 32-bit AMBA system bus connects all components to off-chip SDRAM memory via the SDRAM controller. In the AHB bus, the 8051 microcontroller and the LASP24 core are employed as the master and slave, respectively.

The development of the speech/audio processor is to meet the system demands that are based on sophisticated arithmetic algorithms and that emphasize on both hardware and software solutions. The verified tools offer the opportunity to trade off between software (for flexibility) and hardware (for functionality and performance). The development flow consists of two parts: hardware implementation and software development. These two tools,

Assembler and Emulator, can quickly verify developed algorithms. The assembler can translate LASP24's assembly language into binary codes (or called machine codes). The emulator can emulate the computations of the processor hardware and verify the precision of different floating-point formats such as 32- or 24-bit.

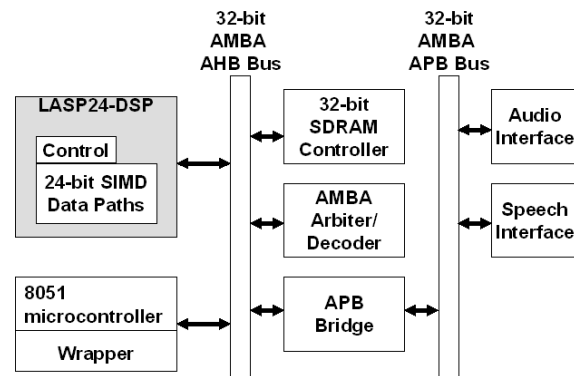


Fig. 1. Architecture of speech/audio codec SOC.

In order to verify and debug the DSP programs, a tool called DEFY-I is developed for functional emulation. The DEFY-I is an instruction-set-level hardware emulator for the processor core. With the emulator, the instructions could be taken out from the program memory and put into the instruction register for instruction analysis and execution. Finally, the execution results are written back to the register file or data memories. The flowchart of DEFY-I is shown in Figure 2. The whole emulator is constructed as the functional simulation kernel and could connect to other peripheral devices to perform the memory and display functions.

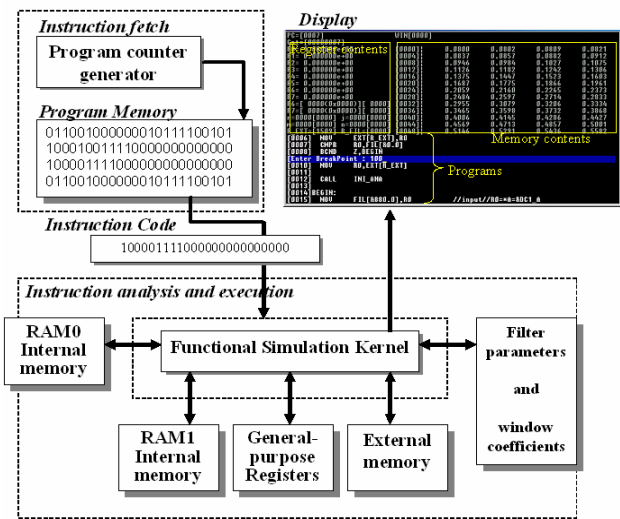


Fig. 2. The structure of DEFY-I for LASP24.

III. Design of LASP24 Core

The LASP24 is a efficiently parallel DSP core with a floating-point operating unit. Floating-point provides fast, accurate, and precise computations. The floating-point format is compatible with 24-bit of IEEE 754 standard. It has a 24-data-path single-instruction/multiple-data (SIMD) processor core controlled by five addressing modes, and a five-level pipeline executing engine. It is important to perform parallel multiplication and arithmetic operations in a single cycle. The effective execution time for most instructions is one cycle.

Figure 3 shows a block diagram of proposed LASP24 core. The core consists of a computation unit, which indicates ALU, multiplier, and accumulators, a program control unit (PCU), an external bus control dictating LASP24 external buses, a vector address generator computing the addresses which are used in vector operations, and two on-chip data memories. The program control unit performs instruction fetch, decoding, exception handling, and wait state supports. The PCU enerators the next address to the program memory and controls hardware loops. The on-chip memory provides an essay data exchange between data paths, which is required for speech/audio processing algorithms.

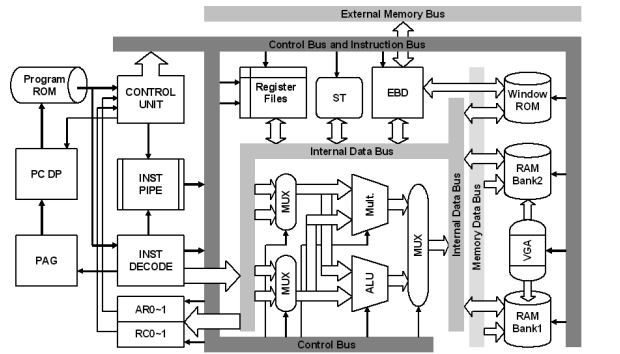


Fig. 3. The block diagram of the proposed DSP core.

LASP24 includes four register groups. The eight general-purpose registers (Register File) are capable of storing and supporting operations on 24-bit floating-point numbers. The two 8-bit auxiliary registers can be accessed by the processor and modified by the auxiliary register arithmetic unit. The primary function of the auxiliary registers is the generation of 8-bit addresses. They can also be used as loop counters or as matrix point register. The status registers contain information relating to the state of ALU and parallel multiplication. When the status registers is loaded, LASP24 sends out a busy signal, and executes the selected function. The two 8-bit repeat counters which used to specify the number of times are to be repeated when performing a block repeat. Concurrently, it has the ability of zero-overhead loop with a single-cycle branch.

A. Instruction Set and Addressing Mode

The ISA of LASP24 is defined as a fixed instruction length at 24 bits. A 24-bit instruction uses five bits each for addressing 8 general-purpose registers, two 3kb internal memories, and one 128kb

external memory. LASP24's instruction set is classified into three groups as data transfer, arithmetic, and control instructions. Each instruction supports 2- and/or 3-operand. The total of defined instructions is twenty-three.

The first group is "data transfer". LASP24 supports one load-and-store instruction (MOV) that can load or store a word (24-bit) between the memory and a register. The second group is "arithmetic and logic". There are 12 arithmetic and logic instructions including floating-point addition (ADD), subtraction (SUB), multiplication-and-accumulation (MAC), matrix multiplication (MPY), logic operations (AND, OR, and SHF), fixed-to-floating (FLOAT), floating-to-fixed (FIX), fixed-point addition (ADDI), and exponential operations (IEXP and EXP). The third group is "control". They control the data flow and perform the functions of no operation (NOP), loading auxiliary registers and filter coefficients (LDC and LDE), repeat and return blocks (RPB and RETB), unconditional branch (CALL), stack operations (PUSH and POP), comparison (CMPR), and conditional branch (BCND).

Most of speech and audio processing is related with auto-correlation, convolution, and FIR calculation. Hence, addressing modes are to enhance the hardware computing capability for the algorithms. Five types of addressing modes allow access of data and instruction words from memory and registers: register, direct, indirect, immediate, and vector addressing modes. Particularly, we design an auto-index method which uses auxiliary registers to address memory data as shown in Fig. 4. This method called vector addressing can easily get memory data in a single multiplier instruction. When the instruction decoder gets the vector address, the address would represent the coordinate of the matrix. Matrix multiplication is based on the operation of RAM0 and R3 (the third general-purpose register). The results are stored to the R3 register. An example for the equation of matrix multiplication is as

$$y = \sum_{j=r-1}^0 x[k, r-j]h[j+1, r].$$

We can replace the above with the following LASP24 micro codes:

```

RPB j, #-1 //set repeat block counter
L1: MOV WIN[j+1, r], R3; //move a coefficient to R3
MPY R3, RAM0[AR0, r-j], R3 //matrix multiplication
ADD R1, R3, R1 //R1=R1+R3
RETB j, L1 //if j≠0, return to L1

```

The index of a matrix coordinate is defined by auxiliary registers (AR0 and AR1). The index can automatically increase so that the pointer indicates the next matrix address. Hence, this addressing method enables a single-instruction matrix computation so that

the size of program memory and the number of program memory access can be reduced.

Additionally, we also define a control mode to control data paths. The control mode is designed for program control and setting of repeat counters. By two auxiliary registers, LASP24 can execute four-level nested program.

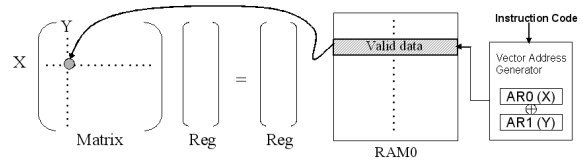


Fig. 4. Illustration for computing a matrix address with the vector addressing mode.

B. Special Vector Processing Techniques

The vector processing scheme [7] provides an approach to accelerating the processing of data streams. This technique can provide a significant speedup for communications, multimedia, and other performance-driven applications by using data-level parallelism. The vector instruction format and addressing representation are shown in Fig. 5.

VC ← VA[AR_A] OP VB[AR_B]									
23~19	18~16	15~14	13~12	11~10	9~8	7~6	5~4	3~2	1~0
OPCODE	011	NU	FIL	EXT	RAM0	RAM1	VC	VA	VB
	FIL	EXT	RAM0	RAM1	VC	VA	VB		
	13~12	11~10	9~8	7~6	5~4	3~2	1~0		
00	FIL	EXT	AR0	AR0	RAM0	RAM0	RAM0		
01	FIL+AR0	EXT+AR0	AR1	AR1	RAM1	RAM1	RAM1		
10	FIL+AR1	EXT+AR1	AR0+AR1	AR0+AR1	EXT	EXT	WIN		
11	FIL-AR0	EXT-AR0	AR1-AR0	AR1-AR0	R3	—	FIL		

Fig. 5. The format of the vector addressing mode and the representation of vector addresses in LASP24, where OP indicates operation; VA, VB, and VC represent vector registers. FIL, EXT, WIN, RAM0, and RAM1 are memory symbols.

A vector multiplication instruction fetches data from RAM0 and RAM1 and feeds into ALU. ALU executes the "MAC" operation and adds the result to the accumulating register. The final results are stored to the external memory. An example of vector processing (100 points) is shown as:

```

L1: MPY RAM0(r), RAM1(r), EXT(r) //EXT(r) = RAM0(r) × RAM1(r)
RETB r, L1 //r=r+1. if r=100, branch to L1.

```

The total execution time is about 200 clock cycles. Hence, we use a single instruction within a repeat block to execute the parallel multiplication-and-accumulation in the auto-correlation operation. The above example demonstrates that LASP24 has higher

performance in vector computation than the general-purpose DSPs.

IV. Physical Design

The processor core was developed by the synthesizable HDL description. The layout view of LASP24 core is shown in Fig. 6. The total gate count is about 30,351 synthesized and estimated with UMC 0.18 μ m standard library (two 1024 by 16 data memories were not included). The silicon area required for this design is approximately 6.5 mm² and the 144-pin CQFP was adopted as the package.

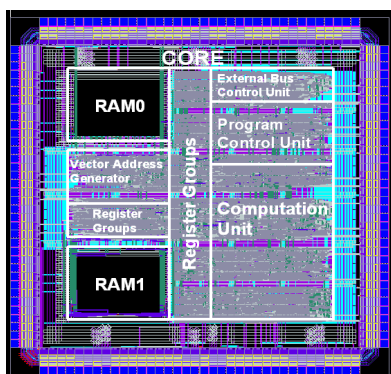


Fig. 6: Layout view of LASP24 core.

V. Results and Analysis

Complexity is measured using million instructions per second (MIPS), random access memory (RAM) and read only memory (ROM) measurements. MIPS are measured using the execution time and instruction counts. Linker memory maps are obtained with required sizes. As Table 1 shows, MELP complexity exceeds LPC and CELP in both processor and memory requirements. Additionally, the total performing cycles is listed for MELP, CELP, and reverberation algorithms.

Now LASP24 can perform the two practice applications in real time. We analyze the performance between them. For the MELP coder, the program performs 1338280 cycles in 60 MHz. The frame size is 22.5ms (180 samples) with a sampling frequency of 8000 Hz. Hence, the latency is about 21 ms (1338280 \times 16.67 ns) for the encoder. As the result for the decoder, the latency is about 9.1 ms. Due to many filters used in the reverberation algorithm, the required execution time is larger. The program performs 1574430 cycles at 80 MHz. The frame size is 22.7 us (stereo channels) with a sampling frequency of 44100 Hz. The latency is about 19.67 us. Anyway, LASP24 can operate max frequency at 100 MHz. By the above analysis, it is able to satisfy all conditions with operating frequency 80MHz.

Table 1. Complexity comparison between processor (LASP24) and memory with optimization codes

Algorithm	MIPS	RAM	ROM	Cycles
		Unit: byte		
MELP Decoder	40	96K	10K	546449
MELP Encoder	60	96K	26K	1338280
CELP Decoder	30	14.8K	128K	364299
LPC	25	1.5K	805	71251
Reverberation	80	96K	30K	1574430

VI. Conclusions

In this paper, the LASP24 core developed for speech/audio codec SOC is presented. It can efficiently perform vector and matrix operations that are not usually supported by general-purpose processors. This design has been integrated in the total area of 6.5 mm² by using UMC 0.18 μ m 1P6M CMOS technology. It has also been demonstrated that the speech coding and audio processing algorithms can be executed on this programmable processor in real-time.

Acknowledgment

This paper was supported by the Brain Research Center, University System of Taiwan, under Grant 92B-711.

References

- [1] H. R. Jang, S. H. Kim, and Y. H. Chang, "A digital signal processor for low power," in *Proc. AP-ASIC*, pp. 42-45, 1999.
- [2] Federal Information Processing Standards Publication (Draft), *Specifications for the Analog to Digital Conversion of Voice by 2,400 Bit/Second Mixed Excitation Linear Prediction*, Jan. 1998.
- [3] M. R. Schroeder and B. F. Logan, "Colorless artificial reverberation," *J. Audio Engineering Society*, vol. 9, 1961.
- [4] ARM Ltd., *AMBA Specification Rev. 2.0*, <http://www.arm.com>, May 1999.
- [5] J. Eyre and J. Bier, "The evolution of DSP processor: from early architectures to the latest developments," *IEEE Signal Processing Magazine*, Mar. 2000.
- [6] M. Dolle, S. Jhand, W. Lehner, O. Müller, and M. Schlett, "A 32-b RISC/DSP microprocessor with reduced complexity," *IEEE J. Solid-State Circuits*, vol. 32, pp. 1056-1066, Jul. 1997.
- [7] C. G. Lee and M.G. Stoodley, "Simple vector microprocessors for multimedia applications," *Microarchitecture, in Proc. 31st Annual ACM/IEEE Int. Symp.*, pp.25-36, Dec. 1998.

ENHANCED V-BLAST PERFORMANCE IN MIMO WIRELESS COMMUNICATION SYSTEMS

Byung Moo Lee and Rui J. P. de Figueiredo,
Laboratory for Intelligent Signal Processing and Communications
University of California, Irvine
byungl@uci.edu, rui@uci.edu

DOI: 10.36724/2664-066X-2022-8-1-25-29

ABSTRACT

Recently, a new detection algorithm for the Vertical Bell Laboratories Layered Space Time (V-BLAST) system, which we call Enhanced-V-BLAST, or simply E-V-BLAST, was proposed. V-BLAST has demonstrated very high spectral efficiency, there is a wide gap between the original V-BLAST algorithm and the Maximum Likelihood (ML) algorithm. Recently, some algorithms have been presented to make narrower this gap. In a new detection algorithm (Enhanced (E) -V-BLAST) for V-BLAST system was presented which showed significantly better performance and flexibility than the original V-BLAST detection. The E-V-BLAST algorithm gets closer to the optimum detection Maximum Likelihood (ML) algorithm by making decisions based on multiple symbols. The Enhanced (E)-V-BLAST has two parameters which can be adjusted to achieve a desired performance and complexity trade-off. In the present paper, we analyze the performance of EV-BLAST as a function of the two inherent adjustable parameters of E-V-BLAST. On the basis of this analysis, we obtain some useful characteristics of the E-V-BLAST algorithm which allow one to achieve the desired performance and complexity trade-off.

KEYWORDS: *E-V-BLAST algorithm, MIMO, Wireless Communication Systems.*

The article is reworked from unpublished 2nd IEEE International Conference on Circuits and Systems for Communications (ICCSC) materials.

The Vertical Bell Laboratories Layered Space Time (V-BLAST) system is a powerful detection algorithm for band-width efficient multiple antenna wireless communication system [2], [3], [4]. Although, V-BLAST has demonstrated very high spectral efficiency, there is a wide gap between the original V-BLAST algorithm and the Maximum Likelihood (ML) algorithm. Recently, some algorithms have been presented to make narrower this gap [1], [5], [7], [8], [9], [10]. In [1], a new detection algorithm (Enhanced (E) -V BLAST) for V-BLAST system was presented which showed significantly better performance and flexibility than the original V-BLAST detection. The E-V-BLAST algorithm gets closer to the optimum detection Maximum Likelihood (ML) algorithm by making decisions based on multiple symbols. The Enhanced (E) -V-BLAST has two parameters which can be adjusted to achieve a desired performance and complexity trade-off. The main idea in E-V-BLAST is that, instead of making an immediate decision on a symbol being detected and cancelled at an iteration step, the decision about that symbol is made at a later level based on the multiple symbol possibilities that have accumulated by descending a tree of width S and depth T .

In what follows, we provide an analysis of the E-V-BLAST system. We analyze the performance of E-V-BLAST and compare the cases of various parameters which we can adjust for performance and complexity trade-off.

The remaining sections are organized as follows. In section II, we address the system model and overview original V-BLAST algorithm. In section III, we present E-V-BLAST algorithm which was introduced recently and analyze its performance. Some simulation studies are shown in section IV. We end in section V by presenting some conclusions.

SYSTEM MODEL

Let M denote the number of transmitting antennas and let N denote the number of receiving antennas in the wireless multiple antenna communication system. The (M, N) single user system under consideration is depicted in Figure 1.

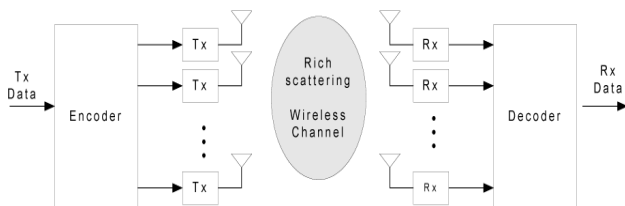


Fig. 1. Block diagram of V-BLAST system

Throughout this paper, we assume $N = M$ for simplicity. It is assumed that there are considerable scattering takes place in the environment and that all the antennas are spaced for uncorrelated fading. We assume perfect channel state information at the receiver. The source

stream is demultiplexed into M substreams, each transmitted from an antenna independently and simultaneously. The received signal r in complex baseband representation can be written as

$$r = Ha + v \quad (1)$$

where v is a complex Gaussian noise vector with zero mean and variance σ_v^2 , a is a transmitted signal vector and H is an $N \times M$ channel matrix whose elements are i.i.d complex Gaussian random variables with zero mean and unit variance.

ENHANCED V-BLAST ALGORITHM

The original V-BLAST embodies the simplest possible solutions. The Enhanced V-BLAST or simply E-V-BLAST algorithm gets closer to optimum detection by making decisions based on multiple symbols. In this section, we review the E-V-BLAST algorithm and conduct an approximate performance analysis. The idea of E-V-BLAST algorithm can be applied to any detection algorithm, detection using Pseudo inverse or QR decomposition. In this paper, we use Pseudo inverse detection for the explanation of E-V-BLAST.

A. E-V-BLAST algorithm

Optimum detection or Maximum Likelihood (ML) detection is computationally very expensive. So, in E-V-BLAST algorithm, we do the following two things.

1. In each of ML detection of the signal based on all M , we make a symbol decision based on T (where $T \leq M$), and continue iteratively.
2. Instead of considering all the possible symbols of our constellation, we consider only the S best (nearest neighbors) symbols.

These two variables, S and T , are adjustable parameters of the algorithm. Their highest possible values are the total number of transmitters for T and the constellation size for S . In this case, detection will correspond to the ML case and will therefore have the highest possible computational complexity. In the simplest case (when $T = 1, S = 1$), the algorithm will be equivalent to original V-BLAST. When a decision is made, the best paths are kept and the rest are discarded.

The E-V-BLAST algorithm is explained with an example in Table 1 where we have initially assumed $T = 2$ and $S = 2$. By choosing $T = 2$ we delay every decision until the following recursion. The choice of S implies that decisions are made based on the combined distance of 2 different transmitter symbols. The two nearest symbols are chosen as shown in Figure 2. We call this operation "Multiple Slicing" and write it as $Q(y_1) = (a_{1,1}, a_{1,2})$, where $Q(y_1)$ denotes the slicing operation resulting in potential candidates $(a_{1,1}, a_{1,2})$. E-V-BLAST also use optimal ordering and DFE like conventional V-BLAST. To completely understand the algorithm, Table 1 should be followed.

Example of detection with E-V-BLAST algorithm, $S = 2, T = 2$ [1]

Column 1	Column 2	Column 3
$r_1 = z_{1,1}a_1 + \nu_1$ <ul style="list-style-type: none"> Form 2 potential candidates symbols (2 nearest neighbors) Find distance metrics corresponding to each symbol Find updated received vectors due to each, using symbol cancellation. 		$y_1 = \mathbf{w}_1^T \mathbf{r}$ $(a_{1,1}, a_{1,2}) = Q(y_1)$ $d_{1,1} = \frac{ y_1 - a_{1,1} ^2}{\ \mathbf{w}_1^T\ ^2}$ $d_{1,2} = \frac{ y_1 - a_{1,2} ^2}{\ \mathbf{w}_1^T\ ^2}$ $\mathbf{r}_{1,1} = \mathbf{r} - a_{1,1}(\mathbf{H})_1$ $\mathbf{r}_{1,2} = \mathbf{r} - a_{1,2}(\mathbf{H})_1$
$r_2 = z_{2,1}\hat{a}_1 + z_{2,2}a_2 + \nu_2$ <ul style="list-style-type: none"> Form total 4 potential candidates. Two assuming $a_1 = a_{1,1}$ and two assuming $a_1 = a_{1,2}$ Find distance metrics for each new potential candidate. Parent node distances are incorporated in the child node distances. These distances are used for decision and pruning of tree. Form updated received vectors due to each new statistic, using symbol cancellation. Decision: Find node corresponding to minimum distance (say $a_{2,3}$). Parent of this node ($a_{1,2}$) is the final detected symbol for previous level (transmitter) Discard undetected parent($a_{1,1}$) and its children 	<p style="text-align: center;">Discard $a_{1,1}$ Choose $a_{1,2}$</p> <p style="text-align: center;">$d_{2,3} = \min$ hence, $\hat{a}_1 = a_{1,2}$</p>	$y_{11} = \mathbf{w}_2^T \mathbf{r}_{1,1}$ $(a_{2,1}, a_{2,2}) = Q(y_{11})$ $d_{2,1} = \frac{ y_{11} - a_{2,1} ^2}{\ \mathbf{w}_2^T\ ^2} + \frac{ y_{11} - a_{2,2} ^2}{\ \mathbf{w}_2^T\ ^2}$ $= d_{1,1} + \frac{ y_{11} - a_{2,1} ^2}{\ \mathbf{w}_2^T\ ^2}$ $d_{2,2} = d_{1,1} + \frac{ y_{11} - a_{2,2} ^2}{\ \mathbf{w}_2^T\ ^2}$ $\mathbf{r}_{2,1} = \mathbf{r}_{1,1} - a_{2,1}(\mathbf{H})_2$ $\mathbf{r}_{2,2} = \mathbf{r}_{1,1} - a_{2,2}(\mathbf{H})_2$ <p>$y_{12} = \mathbf{w}_2^T \mathbf{r}_{1,2}$ etc. Similarly find $a_{2,3}, d_{2,3}, \mathbf{r}_{23}, a_{2,4}$ etc. if minimum distance = $d_{2,3}$ choose $\hat{a}_1 = a_{1,2}$</p>
$r_3 = z_{3,1}\hat{a}_1 + z_{3,2}\hat{a}_2 + z_{3,3}a_3 + \nu_3$ <ul style="list-style-type: none"> After pruning, we have two potential candidates remaining for previous level. Similar situation as in the beginning of row 2 above. Rename, and continue recursively to detect all transmitter symbols. 	<p style="text-align: center;">$\hat{a}_1 = a_{1,2}$</p> <p style="text-align: center;">Renumber if required</p>	<p>Continue recursively, repeat steps above for new tentative symbols. Last symbol remaining at the end is detected based on its minimum distance.</p>

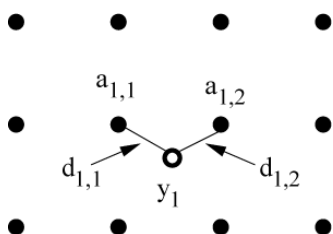


Fig. 2. Multiple Slicing: Choosing two possible candidates for a statistic

B. Approximate Performance Analysis of E-V-BLAST

In this subsection, we approximately analyze the performance of E-V-BLAST system. As we can see in the results of [5], all of signal errors are limited by the worst subchannel or performance of the first signal detection.

$$P[E_j] \leq P[E_1] \cdot \frac{1}{1 - \epsilon}, \quad j = 2, 3, \dots, M \quad (2)$$

where ϵ is very small positive number for large SNR. This is because of inherent error propagation of Decision Feedback Equalization (DFE) in V-BLAST detection. Any detection error in the first signal will most likely re-

sult in detection errors of next signals. If we use feed-forward matrix Q^H , the Hermitian of Q matrix after QR factorization, the elements of channel matrix will have different degree of freedom [5]. If we use pseudo inverse \mathbf{w}_i^T , the post-detection SNR is changed [4]

$$SNR_i = \frac{\langle |a_i|^2 \rangle}{\sigma_v^2 \|\mathbf{w}_i\|^2} \quad (3)$$

We carry out performance analysis of the first signal with i.i.d. Rayleigh fading channel and Additive White Gaussian Noise (AWGN). We use ZF (Zero Forcing)-V-BLAST, so we can regard all of interference is zero, when we detect the first signal of E-V-BLAST.

We define metric as

$$m(r_j, a_j; z_{jj}) = -|r_j - z_{jj} a_j|^2 \quad (4)$$

where z_{jj} is channel matrix component after ZF. We will use Pairwise Error probability (PEP) and union bound for analysis of performance. PEP is defined to be the probability of choosing the nearest signal of a_i , namely, \hat{a}_i , when a_i was transmitted. With perfect channel state information (CSI), PEP can be represented as

$$P_2(a_1 \rightarrow \hat{a}_1 | z_{1,1}) = P[m(r_1, \hat{a}_1; z_{1,1}) \geq m(r_1, a_1; z_{1,1})] \quad (5)$$

If we use Chernoff bound for Q function

$$P_2(a_1 \rightarrow \hat{a}_1 | z_{1,1}) = Q\left(\sqrt{\frac{d_{min}^2 z_{1,1}^2}{4\sigma_v^2}}\right) \leq \exp\left(-\frac{d_{min}^2 z_{1,1}^2}{8\sigma_v^2}\right) \quad (6)$$

Where $d_{min}^2 = |a_1 - \hat{a}_1|^2$. Averaging (6) with respect to $z_{1,1}$ yields

$$P_2(a_1 \rightarrow \hat{a}_1) \leq E_{z_{1,1}} \left[\exp\left(-\frac{d_{min}^2 z_{1,1}^2}{8\sigma_v^2}\right) \right] = \frac{1}{\left(1 + \frac{d_{min}^2}{4\sigma_v^2}\right)} \quad (7)$$

When applying union bound, we should separate error bound in two parts. One part is normal detection and the other part is the effect of E-V-BLAST algorithm.

$$P(E_1) \leq \frac{M_c - S}{\left(1 + \frac{d_{min}^2}{4\sigma_v^2}\right)} + S \cdot P[m_T(\hat{\mathbf{r}}, \hat{\mathbf{a}}; \hat{\mathbf{Z}}) \geq m_T(\hat{\mathbf{r}}, \mathbf{a}; \hat{\mathbf{Z}})] \quad (8)$$

where M_c is signal constellation size and $m_T(\hat{\mathbf{r}}, \mathbf{a}; \hat{\mathbf{Z}}) = -\sum_{j=1}^T |\hat{r}_j - \sum_{i=1}^T \hat{z}_{j,i} a_i|^2$

\hat{r}_j is assumed the received signal after relevant Zero Forcing(ZF) operation for performing ML detection with depth T . One of example of this kind of operation can be found in [5]. More specifically, when $T = 2$, we can represent $\hat{\mathbf{Z}}$ as

$$\hat{\mathbf{Z}} = \begin{pmatrix} \hat{z}_{1,1} & \hat{z}_{1,2} & 0 & 0 & \dots & 0 \\ \hat{z}_{2,1} & \hat{z}_{2,2} & 0 & 0 & \dots & \vdots \\ \hat{z}_{3,1} & \hat{z}_{3,2} & \hat{z}_{3,3} & 0 & \dots & \vdots \\ \vdots & \vdots & \vdots & \ddots & \ddots & 0 \\ \hat{z}_{M,1} & \dots & \dots & \dots & \hat{z}_{M,M-1} & \hat{z}_{M,M} \end{pmatrix} \quad (9)$$

Equation (8) will be clear, if we think about the algorithm.

We choose S signals and delay the decision of these signals in depth T . This means we choose some most error-prone signals S and apply modified ML detection with depth T for the error-prone signals.

The second part of (8) can be

$$P[m_T(\hat{\mathbf{r}}, \hat{\mathbf{a}}; \hat{\mathbf{Z}}) \geq m_T(\hat{\mathbf{r}}, \mathbf{a}; \hat{\mathbf{Z}})] \leq E_{\hat{\mathbf{Z}}} \left(\prod_{j=1}^T \exp\left(-\frac{1}{8\sigma_v^2} \left| \sum_{i=1}^T \hat{z}_{j,i} (a_i - \hat{a}_i) \right|^2 \right) \right) = \frac{1}{\prod_{j=1}^T \left(1 + \frac{d_T^2}{4\sigma_v^2}\right)} = \frac{1}{\left(1 + \frac{d_T^2}{4\sigma_v^2}\right)^T}$$

$$\text{where } d_T^2 = \sum_{i=1}^T |a_i - \hat{a}_i|^2. \quad (10)$$

Finally, we can express the error bound of E-V-BLAST as

$$P(E_1) \leq \frac{M_c - S}{\left(1 + \frac{d_{min}^2}{4\sigma_v^2}\right)} + \frac{S}{\left(1 + \frac{d_T^2}{4\sigma_v^2}\right)^T} \quad (11)$$

where $1 \leq S \leq M_c$ and $1 \leq T \leq M$. S and T are integers.

As we wrote above, the second part of (11) is a kind of ML detection. Therefore, basically what E-V-BLAST algorithm does is using modified ML detection or ML detection with depth T for some signal constellation which is most likely to be in error. According to the equation (11), we may ascertain some characteristics of E-V-BLAST. Increasing S means moving some of most error-prone signals in signal constellation from conventional V-BLAST detection to modified ML detection. Increasing T means improving the performance of modified ML detection part. Increasing S will show good performance at high SNR. But, the effect of increasing S will be reduced as S increased, because of signal constellation structure. The effect of increasing T will be reduced as SNR increases. Because at high SNR, the second term of equation (11) will be ignored, the error performance will be bounded at the first term of equation (11). As we can see, the first term of equation (11) is independent of T . So increasing T will not affect the error probability at high SNR. One more thing we should consider here is that in the highest complexity case ($S = M_c$, $T = M$), equation (11) becomes the usual ML detection.

SIMULATION RESULTS

The E-V-BLAST algorithm was tested by simulation using various S and T for a (5,5) uncoded system. Information symbols are modulated using 16QAM. According to the Figure 3, increasing S significantly improves the performance especially at high SNR. But, the effect of S is reduced as S is increased. This is because of signal constellation structure of QAM. Error usually occurs with right to the nearest neighbors. Increasing S covers the nearest neighbors step by step. So the effect of S is reduced as S is increased.

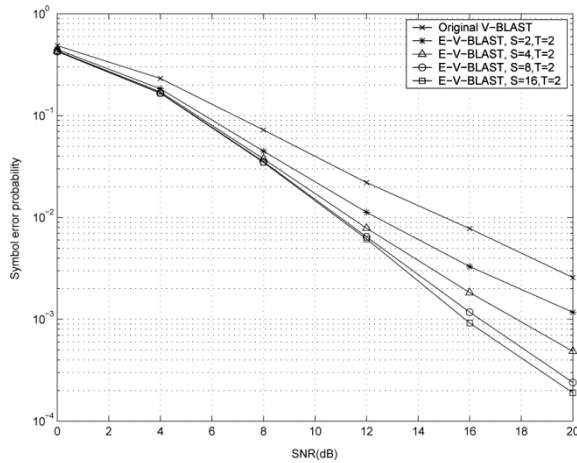


Fig. 3. Performance comparison of E-V-BLAST for increasing S and fixed T , uncoded (5, 5) 16 QAM

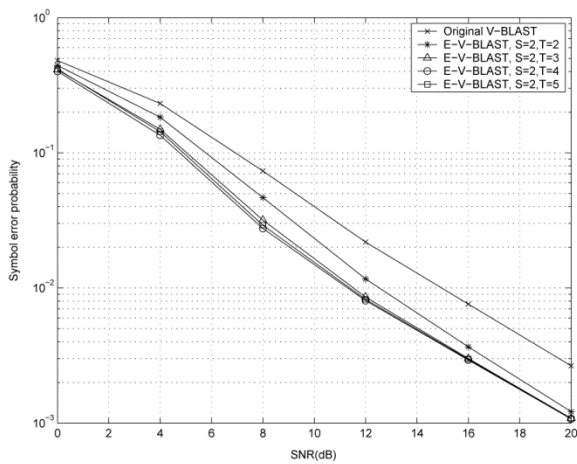


Fig. 4. Performance comparison of E-V-BLAST for increasing T and fixed S , uncoded (5, 5) 16 QAM

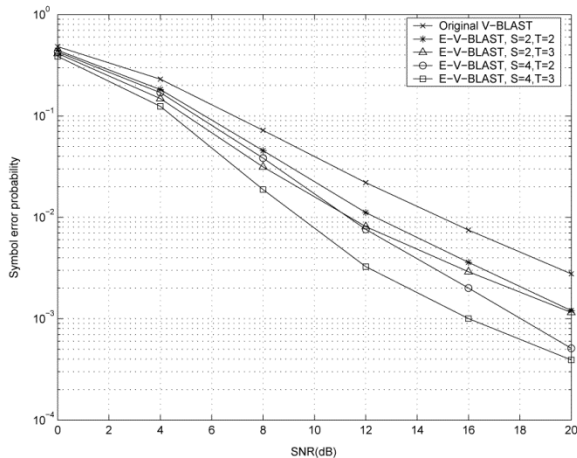


Fig. 5. Performance comparison of E-V-BLAST for increasing T , when S is changed, uncoded (5, 5) 16 QAM

Figure 4 shows at high SNR, the effect of T is not so significant. At high SNR, we can ignore the second term of (11), regardless of the value of T .

In this case, basically, the error probability (11) is bounded in the first term of (11). So all of the system performance of increasing T , but fixed S system will be same at the high SNR. The simulation of Figure 4 is the case of $S = 2$. If S is higher, then the effect of T will be increased. However, as shown in Figure 5, eventually, it also shows same behavior as mentioned above. These results induce us how we can reduce error probability efficiently.

CONCLUSION

We have presented performance analysis of E-V-BLAST and according to this analysis, we found some useful characteristics of the E-V-BLAST algorithm for performance and complexity trade-off. Increasing S is applying ML detection with depth T for some most error likely signals. Increasing T is improving the ML detection with depth T . Increasing T will not affect so much to the performance of E-V-BLAST at high SNR. The importance of increasing T depends on S . That is, the importance of increasing T depends on how many signals will be used for ML detection with depth T . Based on the analysis shown in this paper, we can use relevant level of S and T , depending on circumstances.

REFERENCES

- [1] Ashish Bhargave, Rui. J. P. de Figueiredo and Torbjorn Eltoft. A Detection algorithm for the V-BLAST System, *GLOBECOM 01, IEEE 2001*, Vol 1 pp. 494-498.
- [2] G.J. Foschini. Layered Space-Time Architecture for Wireless Communication in a Fading Environment When Using Multiple Antennas, *Bell Laboratories Technical Journal*, Vol. 1, No 2, pp. 41-59, Autumn 1996.
- [3] G.J. Foschini and M.J. Gans. On the Limits of Wireless Communication in a Fading Environment When Using Multiple Antennas, *Wireless Personal Communications*, Vol. 6(3), pp. 311-335, 1998.
- [4] P.W. Wolniansky, G.J. Foschini, G.D. Golden, R.A. Valenzuela. V-BLAST: An architecture for realizing very high data-rates over the rich-scattering wireless channel, *Proc. IEEE ISSSE-98*, Pisa, Italy, 30th September 1998. IEEE.
- [5] Won-Joon Choi, Rohit Negi, and John M. Cioffi. Combined ML and DFE decoding for the V-BLAST System, *Proc. IEEE ICC-00*, New Orleans, LA, USA, pp.18-22 June 2000.
- [6] John G. Proakis, *Digital Communications*. McGraw-Hill, third edition, 1995.
- [7] D. Wubben, R. Bohnke, J. Rinas, V. Kuhn, K.D. Kammeyer. Efficient algorithm for decoding layered space-time codes, *Electronics Letters*, Vol. 37, Issue 22, pp. 1348-1350, Oct. 2001.
- [8] M.O. Damen, K. Abed-Meraim, and S. Burykh. Iterative QR detection for BLAST, *Wireless Personal Communications*, Vol 19, No 3, pp. 179-192, Dec. 2001.
- [9] Ke Liu and Akbar M. Sayeed. An Iterative Extension of BLAST Decoding Algorithm for Layered Space-Time Signals, *Submitted to the IEEE Transactions on Communications*, Oct. 2002.
- [10] M. Sellathurai and S. Haykin. Turbo-BLAST for Wireless Communications: Theory and Experiments, *IEEE Transactions on Signal Processing*, Vol. 50, pp. 2538-2546, Oct. 2002.

EARTH OBSERVATION AND GLOBAL NAVIGATION SATELLITE SYSTEMS

ANALITICAL REPORT PART I (AVIATION AND SPACE)

Svetlana Dymkova,
Institute of radio and information systems (IRIS), Vienna, Austria,
ds@media-publisher.eu

DOI: 10.36724/2664-066X-2022-8-1-30-41

ABSTRACT

The EU Space Programme is a business growth enabler that stimulates the economy and pushes the bar of innovation. The EUSPA EO & GNSS Market Report is the ultimate guide to anyone who seeks to make the EU Satellite Navigation and Earth Observation technologies part of their business plan and develop new space downstream applications. More than ever society relies on innovative solutions to deal with the big data paradigm. Earth Observation (EO) and Global Navigation Satellite System (GNSS) data is becoming increasingly important to these innovative solutions through dozens of applications that are emerging or already in use by citizens, businesses, governments, industry, international organisations, NGOs and researchers around the world. The study provides analytical information on the dynamic GNSS and EO markets, along with in-depth analyses of the latest global trends and developments through illustrated examples and use cases. Using advanced econometric models, it also offers market evolution forecasts of GNSS shipments or EO revenues spanning to 2031. With a focus on Galileo/EGNOS and Copernicus, the report highlights the essential role of space data across 17 market segments including, Agriculture; Aviation and Drones; Biodiversity, Ecosystems and Natural Capital; Climate Services; Consumer Solutions, Tourism, and Health; Emergency Management and Humanitarian Aid; Energy and Raw Materials; Environmental Monitoring; Fisheries and Aquaculture; Forestry; Infrastructure; Insurance and Finance; Maritime and Inland Waterways; Rail; Road and Automotive; Urban Development and Cultural Heritage; and Space. This article represent the brief overview essential role of space data across 2 market segments including, Aviation and Drones and Rail, Road and Automotive.

KEYWORDS: *GNSS, aviation, space, Low Earth Orbits,*

Brief description based on the Copernicus Programme report, which is coordinated and managed by the European Commission and is the European Union's Earth Observation and Monitoring Programme (www.euspa.europa.eu)

I. INTRODUCTION

For the first time for the European Union Agency for the Space Programme (EUSPA), to introduce the first published EUSPA Earth Observation (EO) and Global Navigation Satellite System (GNSS) Market Report.

The European Global Navigation Satellite System (GNSS) allows users with compatible devices to determine their position, velocity and time by processing signals from satellites. It consists of two elements: Galileo; and the European Geostationary Navigation Overlay Service (EGNOS). EGNOS is Europe's regional Satellite-Based Augmentation System (SBAS). It improves the quality of open signals from the US Global Positioning System (GPS) and (soon) Galileo.

The European Association of Remote Sensing Companies (EARSC) is a not-for-profit organisation which coordinates and promotes the activities of European companies engaged in delivering Earth Observation-derived geo-information services. Acting as a bridge between industry, decision makers and users and covering the full EO value chain (from data acquisition through processing, fusion, analysis and final geo-information products and services), the organisation's members span across 25 countries and include over 130 companies (including SMEs and start-ups) [1].

Coordinated and managed by the European Commission, Copernicus is the European Union's Earth Observation (EO) and Monitoring programme. Copernicus relies on its own set of satellites (Sentinels), as well as contributing missions (existing commercial and public satellites), and a variety of technologies and in-situ measurements systems at atmosphere, land and ocean. The accurate and reliable data generated is turned into value-added information by the Copernicus Services for different thematic domains: atmosphere monitoring; marine environment monitoring; land monitoring; climate change monitoring; and security and emergency management.

Most data generated by Copernicus are made available to anyone globally based on a Full, Free and Open (FFO) data policy. They are accessible through various services, including a set of cloud-based platforms called Data and Information Access Services (DIAS).

The objective of the EU GOVERNMENTAL SATellite COMMUNICATION (GOVSATCOM) initiative is to ensure the availability of reliable, secure and cost-effective satellite communication services for EU and national public authorities managing emergency and security-critical missions, operations and infrastructures.

2021 has been a year of accomplishments for the European Union in space. The first-ever integrated Space Programme, gathering the two satellite navigation systems, Galileo and EGNOS, the EU Earth Observation system, Copernicus, and GOVSATCOM, the upcoming system for secure governmental communications, is now in place. EUSPA has an extended mandate, including the provision of satellite-based services for Galileo and EGNOS and

development of the GOVSATCOM Hub, enhanced security responsibilities, and the market uptake of Galileo, EGNOS, commercial utilization of Copernicus, and the development of GOVSATCOM users' phase, among others.

A strategic goal of the European Commission (EC) space strategy is to reinforce Europe's strategic autonomy in accessing and using space, and this in a secure and safe environment.

Since its inception, the report has established itself as the most authoritative reference document for information on the global GNSS market.

II. GNSS DOWNSTREAM SPACE APPLICATION MARKET

Earth Observation (EO) refers to remote sensing and in-situ technologies used to capture the planet's physical, chemical, and biological systems and to monitor land, water (i.e. seas, rivers, lakes) and the atmosphere. Satellite-based EO by definition relies on the use of satellite-mounted payloads to gather data about Earth's characteristics. As a result, satellite-based platforms are suitable for monitoring and identifying changes and patterns for a range of physical, economic, and environmental applications globally. Once processed, EO data can be assimilated into complex models to produce information and intelligence (e.g. forecasts, behavioural analysis, climate projections, etc.), and complemented by in-situ measurements.

Firstly, different types of sensors utilize different EO technologies:

- *Optical or thermal sensors* are payloads monitoring the energy received from the Earth due to the reflection and re-emission of the Sun's energy by the Earth's surface or atmosphere. They operate between the visible and infrared wavelengths of the electromagnetic spectrum.

- *Radar sensors* are payloads operating in the lower part of the spectrum (longer wavelengths). Most of these sensors send energy to Earth and measure the feedback from the Earth's surface or atmosphere, enabling day and night monitoring during all-weather conditions.

The second essential parameter in EO is the sensor resolution.

- *Spatial resolution* defines the size of the pixels analysed by the sensors. EO satellites can be distributed into three categories based on this parameter: Low and medium resolution, High resolution, and Very-High Resolution.

- *Temporal resolution* defines the frequency at which the data is acquired for a defined area. The needs can vary substantially for this parameter, with applications requiring images every day or every few hours, whilst others require updates only every few weeks.

Spectral resolution is also considered in the case of optical sensors. This is defined by the width of the spectrum bands that can be distinguished by the payload, enabling some applications that require the ability to analyse specific wavelengths.

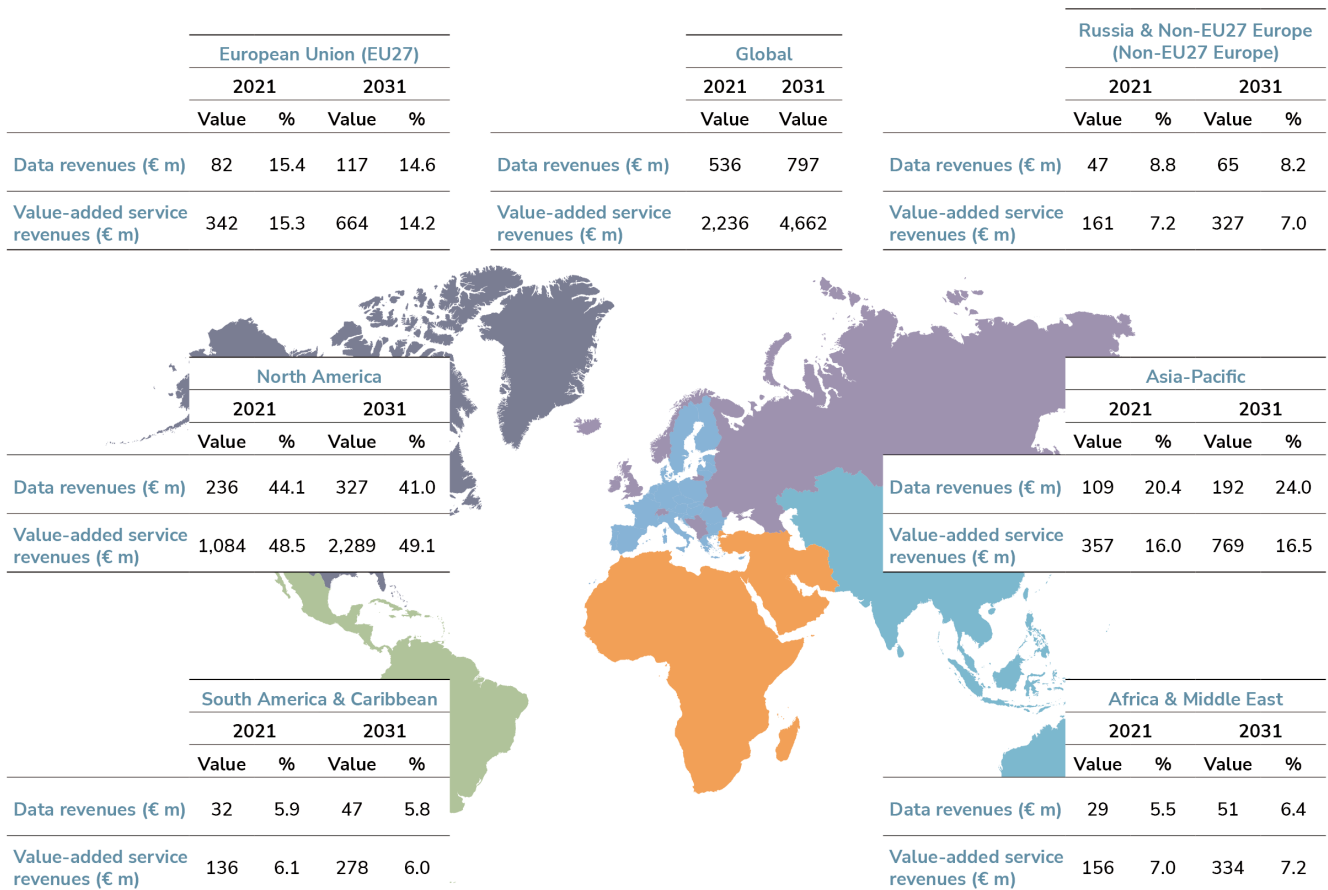


Figure 1. EO demand world map

Copernicus delivers accurate and reliable information in the field of environment and security and supports a wide range of Union policies in domains such as agriculture, environment, energy, health, civil protection, humanitarian aid and transport. Mainly tailored to the needs of public authorities, Copernicus also serves research, academic, commercial and other private users. The system consists of three main components: a space component, which delivers data from a fleet of dedicated observation satellites (the 'Sentinels') and from contributing missions; an in-situ component which collects data acquired by a multitude of sensors at air-, sea- and ground-level; and a service component which transforms the wealth of satellite and in-situ data into timely and actionable information products.

The programme is managed by the European Commission and implemented in partnership with the Member States, European Space Agency (ESA), European Organisation for the Exploitation of Meteorological Satellites (EUMETSAT), European Centre for Medium-Range Weather Forecasts (ECMWF), EU Agencies and Mercator Ocean International.

The Sentinels are the Earth Observation satellites dedicated to the Copernicus programme and are designed to meet the needs of the Copernicus services and their users. Made-up of six families, they ensure an independent and autonomous Earth Observation capacity for Europe with

global coverage. They deliver observations (including day and night, all-weather observations) which serve a wide range of user needs related to land and ocean surfaces, atmospheric measurements, air quality, emergency situations, and so on.



- Sentinel-1A & -1B provide all-weather, day and night radar imagery for land and ocean services.

Sentinel-3A & -3B provide optical, radar and altimetry data for marine and land services.

- Sentinel-6 provides radar altimetry data to measure global sea-surface height, primarily for operational oceanography and for climate studies.

- Sentinel-2A & -2B provide optical imagery for land and emergency services.

- Sentinel-5P provides atmospheric data, bridging the gap between Environmental Satellites (ENVISAT) and future Sentinel-5 data.



- Sentinel-4 and 5 are payloads to be respectively embarked aboard EUMETSAT MTG-S and Metop-SG satellites, in order to provide data for atmospheric composition monitoring (to be launched early 2024).

Radio Navigation Satellite Services (RNSS) is infrastructure that allows users with a compatible device to determine their position, velocity and time by processing signals from satellites. RNSS signals are provided by a variety of satellite positioning systems, including global and regional constellations and Satellite-Based Augmentation Systems:

Global constellations i.e. Global Navigation Satellite System (GNSS): GPS (USA), GLONASS (Russian Federation), Galileo (EU), BeiDou (PRC).

- Regional constellations: QZSS (Japan), NavIC (India), and BeiDou regional component (PRC).

- Satellite-Based Augmentation Systems (SBAS): WAAS (USA), EGNOS (EU), MSAS (Japan), GAGAN (India), SDCM (Russian Federation) and SNAS (PRC).

This Market Report considers the GNSS market defined as activities where GNSS-based positioning, navigation and/or timing is a significant enabler of functionality. The GNSS market presented in this report comprises device revenues, revenues derived from augmentation and added-value services, (which together form 'Services') attributable to GNSS.

Augmentation services include software products and content such as digital maps, as well as GNSS augmentation subscriptions. Added-value service revenues include data downloaded through cellular networks specifically to run location-based applications (such as navigation), as well as the GNSS-attributable revenues of smartphone apps (sales revenue, advertisements and in-app purchases), subscription revenues from fleet management services, drone service revenues across a range of industries, and so on. Both services are shown on the World Map (next page) together as 'Services'.

For multi-function devices such as smartphones, the revenues include only the value of GNSS functionality - not the full device price. Therefore, a case-specific correction factor is used:

- GNSS-enabled smartphone: Only the value of GNSS chipsets is counted.

- Aviation: The value of the GNSS receiver inside the Flight Management System is taken into account, in addition to the GNSS-specific revenues driven by the certification process.

- Precision Agriculture system: The retail value of the GNSS receivers, maps, and navigation software is counted.

Search and Rescue devices: For Personal Locator Beacons and Emergency Locator Transmitters, only the price differential between GNSS and non-GNSS devices is included.

Global annual GNSS receiver shipments will grow continuously across the next decade (from 1.8 bn units in 2021 to 2.5 bn units in 2031). The vast majority are associated with the Consumer Solutions, Tourism and Health segment which contributes roughly 92% of all global annual shipments thanks to the enormous numbers of smartphones and wearables being sold on an annual basis. From a regional point of view, it is clear that Asia-Pacific will continue its reign as the largest market.

The overall installed base will grow from 6.5 bn units in 2021 to 10.6 bn units in 2031. Similar to global shipments, the lion's share of the installed base is dominated by the Consumer Solutions segment, accounting for 89% of global GNSS devices in use for 2021 and 86% in 2031. This drop of 3% in global share over the next decade is mainly influenced by the declining share of smartphones across all GNSS devices as there is a global trend towards extending the useful life of a smartphone, which in turn translates into a decrease in smartphone shipments. In parallel, the growing adoption and integration of In-vehicle Systems amongst new car shipments pushes the share of the Road and Automotive segment amongst the global installed base of GNSS devices from 9% in 2021 to 12% in 2031.

Looking at other segments (graphs in the bottom-right), Aviation and Drones is a significant market expected to grow from 42 m units in 2021 to 49 m in 2031. The Maritime segment is the second largest market in 2021, but sees its global share of 17% in 2021 (corresponding to 11 m units) drop to 16% (17 m in 2031), whilst Agriculture becomes the second largest market reaching a share of 18% in 2031 (roughly 20 m units in 2031, up from less than 5 m units in 2021).

The global GNSS downstream market revenues from both devices and services will grow from 199 bn in 2021 to 492 bn in 2031 with a CAGR of 9.2%. This growth is mainly generated through the revenues from added-value services. Combined, services revenues (i.e. both added-value services and augmentation services) will account for 405 bn in 2031, more than 82% of the total Global GNSS downstream market revenues.

Road and Consumer solutions dominate all other market segments in terms of cumulative revenue with a combined total of 90% for the forecasting period 2021-2031.

In the Road sector, most revenues are generated by devices used for navigation (In-Vehicle Systems (IVS)), emergency assistance, ADAS as well as fleet management applications (including insurance telematics), whereas Consumer Solutions revenues mainly come from the data revenues of smartphones and tablets using location-based services and applications.

The adjacent table shows the regional market shares for Components and Receiver manufacturers in 2019 for each market segment. The data are created using the methodology described on the previous page. European companies account for a quarter of the global GNSS Components and Receiver manufacturers market in 2019 (compared to 27%

in 2017). The European industry's market share in this value chain category varies across market segments. While it has above average market shares in segments such as Road (53%), Maritime (47%) and Space (65%), it has below average market shares in segments such as Consumer Solutions (7%), Aviation (17%), Rail (14%), and Drones (10%) (Table 1).

Table 1

Europe's 2019 market share in Components & Receivers, by market segments

	Europe	North America	Asia +Russia		Europe	North America	Asia +Russia
Consumer Solutions	7%	45%	47%	Agriculture	20%	47%	33%
Road and Automotive	53%	25%	22%	Geomatics	35%	31%	33%
Manned Aviation	17%	81%	2%	Emergency Response	33%	39%	13%
Rail	14%	15%	71%	Drones	10%	42%	48%
Maritime	47%	27%	26%	Critical Infrastructures	36%	50%	12%
Space	65%	19%	17%				

Note: Segment share for Rest of the World is not shown in this table.

III. AVIATION AND DRONES

Aviation is one of the main drivers behind increasing global connectivity. In comparison, drones are a relatively recent technology which can put a payload anywhere it is needed. The aviation and drones segment encompasses services and products used by aviation and drone operators and industry. This includes airlines, pilots, helicopter operators, drone operators, airports and air navigation service providers.

Aviation uses GNSS extensively, with Satellite-Based Augmentation Systems (SBAS) providing better access to small and medium airports through Performance Based Navigation procedures, increasing safety and enabling business growth across Europe. GNSS is the primary source of navigation for aviation and drones, and meets the present-day performance requirements for all airspaces, from low-level to sub-space. GNSS supports advances in urban air mobility with evaluation of flight risk (e.g. geofencing, populated area avoidance, landing site optimisation), automation and tracking through position self-reporting (known as Electronic Conspicuity).

Combining GNSS and EO data advances emissions monitoring systems. EO itself enables the monitoring of volcanic ash clouds, emissions, terrain (supporting optimised routing), flight procedure development and flight planning. This benefits airlines, leisure pilots, drone operators, airports, air traffic control and public agencies serving global aviation communities.

In the context of the new European regulations¹ on drones, there has also been a push toward supporting systems that are able to help monitor the positions of drones and to provide a service that supports access to airspace without relying on temporary segregation techniques that can inconvenience other airspace users. This depends on the

deployment of GNSS as the only ubiquitous Position Velocity Time (PVT) solution available in drones due to size and power constraints - and is also the case for certified drones, although they may also depend on traditional terrestrial based aviation solutions.

These applications enabling drone traffic management are also underpinned by GNSS positioning on smartphones and within the drones themselves. This supports the planning and execution of missions. These operate similar to the 'moving map' applications used today by manned aviation and are designed to help users understand and avoid temporary and permanent airspace restrictions.

The planning and execution of missions also needs to account for operation risk based on location, such as obstacles to aviation in the vicinity, risks from overflight, and proximity to people and property. This relies on accurate, up-to-date information which itself can be dependent on frequency of satellite-based mapping and identification of specific features.

Earth Observation data supports GNSS based applications

All aviation depends on reliable positioning information, both in terms of current location and direction of travel. GNSS has made this information more intuitive across the whole industry, especially with the introduction of moving map displays. At International Civil Aviation Organisation (ICAO) level the requirements for terrain and obstacle data to be available electronically have started to shift focus toward utilising satellites for data acquisition. Today, this satellite-derived topographical data enables all flight procedure analysis, particularly with regard to safety in relation to any proximate terrain or obstacles.

Further benefits have been realised in the aftermath of volcanic eruptions, showing the value of utilising satellite data to avoid ash clouds, protecting aircraft engines from possible inflight failure. GNSS proves equally relevant and beneficial in the industry from an environmental perspective, supporting assessment of aviation emissions and sustainability and local aerodrome impacts such as land and flooding risks, airfield air pollution and environmental planning.

The use of EO coupled with GNSS-derived data by drones supports collision and population risk assessments and is more important in the more dynamic environment in which drones may operate compared to traditional aviation. More frequently updated datasets, derived for aviation purposes, are essential to allow planning of aviation infrastructure, development of databases for map-based systems (e.g. moving maps, Unmanned Aircraft System Traffic Management (UTM) and terrain avoidance systems) coupled with GNSS data for positioning in relation to maps, flight procedure design and surveillance infrastructure. Procedure design and placement of surveillance infrastructure such as radars, terrain and obstacles (trees, buildings, etc.) are essential information that is used in pre-implementation assessments.

Within the aviation segment, European and North American organisations continue to dominate manufacturing of GNSS receivers for aviation (>95% of the market) in 2019 with North American receiver suppliers supplying 85% and European suppliers 14%.

The picture is more mixed when it comes to drones, with shares depending on the sophistication of the drone platform. Overall the Asian share is 47% with the European share at 10%.

GNSS capabilities are growing to meet evolving requirements for navigation, surveillance and sustainability (figure 2).

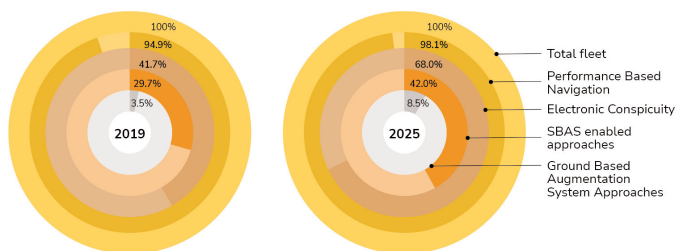


Figure 2. GNSS capabilities as a proportion of total civil aviation fleet

Dual Frequency Multi-Constellation progress in navigation

The GBAS Approach Service Type D (GAST D), which allows Cat-III precision approaches to less than 100ft height, is fully standardised and validated for GPS L1 signals. Furthermore, a dedicated ICAO ad-hoc group is defining the future DFMC GBAS concept, which takes benefit from dual-frequency signals and multiple constellations such as GPS and Galileo, in order to enhance the robustness of GBAS approach service and even explore new GBAS services. The ICAO DFMC GBAS Concept Paper is expected by the end of 2022.

As of today, it is expected that the GNSS Manual (Doc 9849) will update to accommodate GAST-F in 2024 and that ICAO Standards And Recommended Practices for GBAS GAST F would be written around 2030.

GBAS GAST F or GBAS DFMC is seen as the future of GBAS and will enable greater robustness against ionosphere disturbances as well as against Radio Frequency Interference (RFI), as it will work with two frequencies and offer reversion modes.

The ICAO Navigation System Panel (NSP) approved new Standards and Recommended Practices for the use of EGNOS and Galileo in November 2020. This is an important milestone in SBAS DFMC Standardisation for EGNOS and Galileo but also for European aviation. Indeed, DFMC SBAS opens up new possibilities for air transportation but also more resilience for users against RFI.

In the U-Space and UAM area EUSPA has supported numerous trials of drones equipped with EGNOS as well as Galileo through its EGNSS4RPAS project. Manned air-

craft are expected to be outnumbered by all kinds of drones, employed for everything from weather and environmental monitoring to personalised delivery services. The traditional person-based air traffic control model will need to evolve to accommodate such a shift, based on automated monitoring, traffic management and collision avoidance. In Europe, this highly automated version of air traffic control is termed U-Space.

GNSS performance requirements supporting drone operations are being developed globally. Eurocae WG-105 within Europe is developing minimum operational performance specifications (MOPS) for Detect and Avoid (DAA) in Very Low Level (VLL) airspace.

SBAS's safety-of-life service is essential to making this happen, moving from today's situation - where drones are limited to specific air corridors and line-of-sight operations - to let them roam freely but safely in busy airspace and built-up areas.

Electronic Conspicuity is an umbrella term for technologies that provide self-reporting of position from an aircraft to other aviation actors. Electronic Conspicuity can be considered in two groups: Certified (used in controlled airspace by users such as commercial aviation and certified category drones) and Uncertified (used outside controlled airspace typically by General Aviation). It is also an essential enabler for U-Space as the means to provide the ability to 'detect' other aircraft. No solution has yet been agreed to enable interoperability between U-Space and manned aviation, but GNSS positioning reporting is enabled through the established ADS-B and a mix of proprietary solutions gaining traction with some users. There are several solutions including Automatic Dependent Surveillance Broadcast (ADS-B) (1090MHz and UAT), Flight Alarm (FLARM), LTE/5G and 802.11 raising questions on interoperability.

ADS-B implementation, both airborne equipment and ground infrastructure, continues toward full integration in the ATM environment. Since December 2020, new aircraft are required to be ADS-B equipped with a transition period till June 2023 for retro-fit. At European level, users would like to improve cost-efficiency through rationalisation of the surveillance infrastructure, including the decommissioning of CNS facilities and to improve the aviation spectrum efficiency. GNSS will become more critical as this step progresses.

The exploitation of GNSS timing as a reference source for timing and synchronisation processes is fundamental for critical infrastructure like telecommunication networks, energy distribution grids, financial markets and commercial aviation systems and networks.

In the case of aviation, optimising the traffic flows also comes down to timing, as does synchronisation of information about flights. This information can be shared between users to cut down on flight times and reduce delays, diminishing the environmental impact. GNSS time is used for:

- positioning and timing for on-board navigation purposes;

- timing and synchronisation for datalink communications (on-board to ground and vice-versa); and timing and synchronisation for ground systems used for Air Traffic Control (ATC), communication networks, airspace surveillance, and airport logistics coordination.

Aviation needs advanced GNSS and new alternative PNT solutions

Traditional aviation has always operated with alternative technologies, particularly ground-based navigation aides, in addition to GNSS. Whilst these technologies cannot deliver the performance equivalent to GNSS, particularly with DFMC, they do provide resilience.

With interoperability, new airspace users expect a continued push for rationalisation of historical alternative technologies in the future, there will be a need to maintain a spectrum and cost-efficient solution accessible to all, drones and manned aviation alike. Technologies such as the L-band Digital Aeronautical Communications System (LDACS) and 5G offer integrated positioning services, yet there is no clear solution that can meet the key performance requirements that GNSS delivers.

In 18th November 2020, EUSPA and EHA (the European Helicopter Association) hosted a workshop on the GNSS/EGNOS benefits for Helicopter Emergency Medical Services (HEMS) operations. This builds on the increasing importance of GNSS to support helicopter operations operating in hostile environments, such as close to mountains or in valleys with poor connectivity to traditional infrastructure.

In addition, the use of GNSS-based altitude can provide specific benefits for helicopter operations under particular conditions:

- GNSS-based altitude can be used instead of barometric altitude to improve altitude information reliability in low-level operations in areas where the local settings for barometric altitude (QNH) are not available or not reliable.
- Terrain Awareness Warning Systems (TAWS) and Synthetic Vision Systems (SVS) data is based on GNSS altitude. If the altitude displayed in the helicopter cockpit were GNSS-based instead of barometric, then all data would have the same reference and be coherent.
- At low speeds, the rotor flow can impact barometric sensors, which can lead to some bias on barometric altitude determination. On some helicopters, a hybridization of GNSS-based altitude with barometric altitude is already made to reduce noise and bias in the altitude value.

The global drone market will grow from 19.4 bn in 2020 to over 36.9 bn in 2025 at a CAGR of 13.8%1.

This huge growth will drive shipments of GNSS-capable drones to exceed 10 million units per year for most of this decade, as shown in the chart below. The proportion of drone service revenue attributed to GNSS is shown in the adjacent chart. Nearly all drone use cases will continue to be operated outside of controlled airspace by Open or Specific

category drones. Certified Electronic Conspicuity and Performance Based Navigation devices will be used for high-value applications, but by a relatively small population (compared to the overall drone market) of Certified drones.

Applications such as critical infrastructure inspection and drone Delivery & eCommerce - which is predicted to be the largest market area by 2030 - are developing rapidly. These applications increase demand for Beyond Visual Line of Sight (BVLOS) missions classified as medium risk, which will fall under the Specific category. Such missions require a proportionate approach to safety and will require a design verification report. The designs will almost certainly include Electronic Conspicuity devices (uncertified as they will be outside of controlled airspace) to ensure awareness of other airspace users, and support U-space tracking by UTM systems.

Urban Air Mobility (UAM) is a concept looking for ways to quickly and efficiently move people within cities in a safe and environmentally friendly manner. UAM transport networks will offer an alternative to congested city transport systems and will develop strong interfaces between city/region, drone, transport and urban planning communities. UAM is expected to debut in the coming years in big cities such as Paris and Singapore, according to Volocopter and Lilium, two European leaders in this market. UAM is not expected to emerge as a significant market until the 2030s.

As in most transportation modes, UAM strongly benefits from the GNSS services for positioning, but also from other services that are specifically tailored to drones applications: geo-fencing and geo-caging; e-identification (Drone navigation and guidance); and tracking (facilitated via Electronic Conspicuity). Maps that integrate EO data will provide up-to-date information about the distribution of dwellings and approximate population. This will help planning routes for UAM traffic to avoid densely populated areas and for developers to strategically plan infrastructure.

The Solution for EGNSS U-Space Service (SUGUS) project, funded by the European Commission, organised a survey last year, whose results can be used as a valuable input to tailor the EGNSS Service Provision layer to specific drone missions' needs, allowing better mitigation of risks in complex operations like UAM, increasing safety and security.

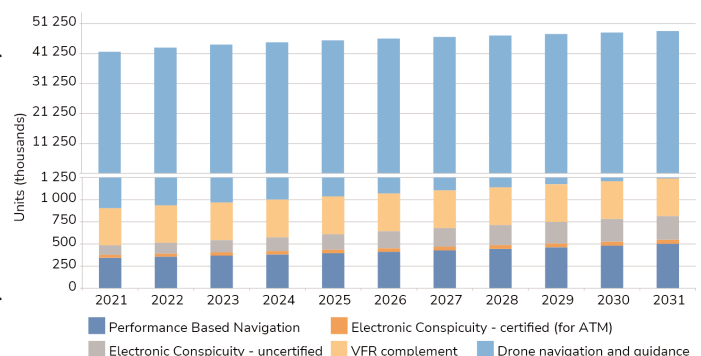


Figure 3. Installed base of GNSS devices by application

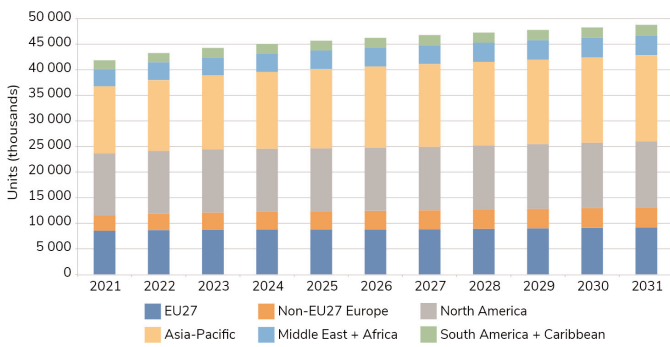


Figure 4. Installed base of GNSS devices by region

Successful economic development of the Arctic zone is impossible without the creation of a continuous information field covering its entire territory and accessible not only on stationary objects, but primarily on mobile vehicles - ships, vehicles, aircraft, etc. [9,10] The information field means the transmission of audio information (broadcasting programs), data (weather maps, ice conditions, etc.), navigation signals, alerts and information about emergencies, as well as other service information in the interests of various departments. Given the harsh climatic conditions, the reliability of information support directly determines the safety of human life in the Arctic. To ensure the required level of reliability, it is necessary to use at least two parallel operating and duplicating each other systems - the main and backup, based on different principles of operation.

Obviously, the information support of mobile objects can only be implemented using various radio systems. (Solutions for stationary objects are more diverse and are not considered in this article). It is also clear that, in most cases, large-sized and spatially oriented antenna systems cannot be installed on mobile objects. For this reason, even in the middle part of the Arctic zone (at latitudes above 75° and up to 81°), where the geostationary orbit (GSO) is observed very low above the horizon and only a small part of it is visible, on which satellites of the necessary operator are not always present, providing information field using GSO

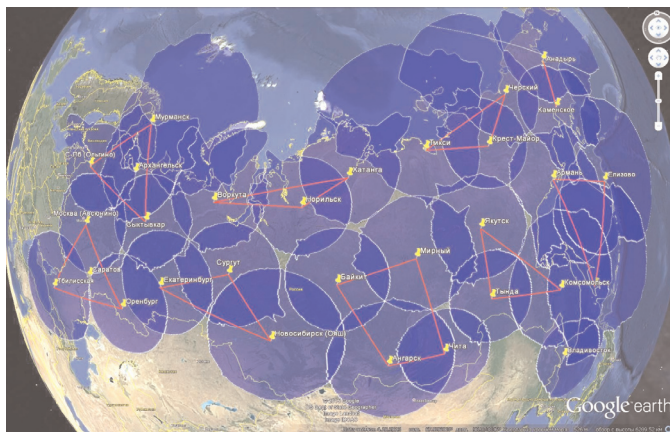


Figure 5. An example of the state digital radio broadcasting network architecture of Russia in LF range

satellites is not possible. From approximately 81° to the poles, the GSO is not visible from the Earth's surface, even theoretically.

The most promising for the formation of the main information field in the Arctic zone can be considered satellite systems located in highly elliptical or low orbits. At the same time, the high cost of such systems, the long period of infrastructure deployment and limited service life, combined with the low population density in the service area, determine their planned unprofitability and the need for budget financing.

As a backup means of forming the information field, it is advisable to consider terrestrial digital broadcasting systems [5-8]. By providing broadcast data rates comparable to those available for omnidirectional antenna reception in satellite systems, modern terrestrial digital broadcasting systems can be significantly more economical to deploy and operate. Prior to the commissioning of the satellite segment (in HEO or in low orbits), ground facilities can successfully perform the function of forming the main information field.

Many countries have chosen the European digital broadcasting technology platform, the digital broadcasting or digital sound broadcasting and DRM systems. Was investigated the possibility of using the DRM system at frequencies below 30 MHz. The completed studies confirmed the standard specifications for digital broadcasting or digital sound broadcasting and DRM systems [11-13].

IV. SPACE

Although GNSS was originally designed to serve terrestrial users, it has also proven its worth as a valuable tool in space. Within the last decade the space industry has experienced a profound transformation. Driven by technological advancements and a new entrepreneurial spirit, the space environment is now hosting an increasing number of platforms and has therefore become a new playground for GNSS technologies.

Whatever the mission type (telecommunication, Earth observation, scientific development, navigation, etc.), providing reliable real-time GNSS data to Earth-orbiting satellites can bring many financial, technical and societal benefits such as reduced mission costs, improved navigation performances and the provision of trustworthy EO data.

The launch of Low Earth Orbits (LEO) megaconstellation projects has become a symbol of this new era, showcasing incredibly diverse commercial possibilities such as EO in particular, but also in Satellite Communication for broadband connections and the Internet of Things (driven by the needs of global coverage and low latency). This phenomenon is inevitably leading to an unprecedented number of satellites orbiting the Earth and calls for new performance needs. GNSS has a major role to play in this evolution, thanks to the financial and technical benefits it brings (e.g. reduced number of instruments, reduced dependence on ground-based stations, improved navigation performances,

etc.) and its applicability to both historical and emerging stakeholders.

Entering the third millennium, about 800 satellites were actively orbiting the Earth. Twenty years later, this number has exceeded 3,500 satellites and is expected to quadruple over the next decade. Outer space has become unbelievably crowded and the risk of collision between space objects statistically increase with every new launch.

Although all space users operate in a similar environment - i.e. outer space - many variables actually come into play when identifying case-to-case GNSS requirements.

Depending on their characteristics (e.g. mass, designed lifespan, mission type, mission costs, etc.) and the orbit they are targeting (due to variable geometrical constraints and signal availability), spacecraft are indeed not expected to be equipped with the same kind of spaceborne GNSS receivers. At relatively low altitudes (3,000- 8,000 km), GNSS receivers generally benefit from a good signal availability from any single constellation.

On the contrary, high altitude (8,000-36,000 km) are much more challenging as they often have to cope with a significantly reduced GNSS signal availability and therefore need ultra-sensitive receivers (i.e. able to exploit GNSS signals first side lobes) which are at the cutting edge of current technology. Also, large satellites can embark relatively heavy receivers (a few kilogrammes) while SmallSats must avoid this extra mass. Similarly, most CubeSat missions cannot afford expensive pieces of equipment while long-term missions are ready to do so to guarantee system robustness.

To tackle the space debris issue and avoid its escalation, mitigation measures and remediation services are today being considered and entrusted to the EU SST Consortium through the new Space Regulation. From the definition of post-mission disposal guidelines, to regular spacecraft evasive actions or the development of cutting-edge space debris removal technologies (e.g. robotic arms, harpoons, nets), some of these measures require the use of accurate positioning systems, representing a real opportunity for the spaceborne GNSS market.

The Astroscale ELSA-M spacecraft which aims, for example, to remove multiple retired satellites from LEO in a single mission, will use the off-the-shelf 'Constellation On Board Computer' (cOBC) GPS and a Galileo-enabled RUAG GNSS receiver. Astroscale announced a funding award from OneWeb, to mature their technology and capability towards a commercial service offering by 2024.

In 20 years, such systems might be used to bring space debris into dedicated recycling stations, in order to reuse part of their materials and components - these will rely on Galileo- based positioning systems.

Europe dominates the market for GNSS Components and Receivers, with a share of 73%, ahead of North America's 21%, in 2019, thanks to a combination of both historical stakeholders and new actors answering NewSpace needs. Led by Airbus, Hexagon and U-Blox, European

companies hold six of the top 10 positions among manufacturers in the market.

Resulting from an ever-increasing adoption of GNSS-based solutions among the space users and the continuous development of new megaconstellation projects, the number of spaceborne GNSS receivers to be sold is expected to progressively increase in the coming years. The variable levels of certainty on the long-term success of these megaconstellations however prevent from properly assessing their potential replacement cycles and the impact it could have on the market on the second part of the decade.

High-end receivers are and will probably remain for the next decade the main option for most Space applications (except for technology development, due to their high cost). Yet, it is expected that Low-end receivers - which are today mainly used to support specific scientific or operational satellite missions, or for space timing and synchronisation - may significantly expand to Attitude Determination and Precise Orbit Determination applications, covering a growing part of LEO needs. As of today, two reasons suggest that these estimations with of future Low-End unit sales are conservative. First, only megaconstellations with granted FCC filings were captured within the model and no satellite replacement was included. Second, the CubeSat market might be slightly underestimated, since reliable data on forecasted university/academia missions are not available.

New actors are however not expected to replace historical ones, but to challenge and complement them. The technological push that has always defined the space industry is now strengthened by the user pull generated by new stakeholders' arrival and the need they create. Most of the new small LEO satellites are coming out with a need for GNSS receivers. With a relatively short lifetime and therefore a higher replacement rate, these satellites stand as the key driver of the spaceborne receivers' market. The technical adaptations required to evolve in this space environment are well-known and technically mastered in these low-altitude regions. The GNSS market for LEO satellites is therefore mature and several companies already propose off-the-shelf products (e.g. SSTL, GOMspace, Thales Alenia Space, etc.).

Software-defined receivers constitute a very interesting approach for space users, offering features such as re-programmability (i.e. upgradeability) or self-healing capabilities. The most vivid examples could be the possibility to upload algorithms yet-to-be-invented at the receiver's launch time, or the ability to recover from a single-event effect by remotely rewriting damaged functionalities, reducing the need of onboard redundancy.

Launched late 2017 by the GSA and led by Qascom, the ENSPACE (Enhanced Navigation in Space) project has recently developed an innovative GNSS spaceborne receiver. Targeting the needs for robust positioning, navigation and timing of satellites with the flexibility of a software solution, the ENSPACE technology fosters the use of GNSS in

space. Configurable for multiple applications (e.g. navigation in space, timing determination, precise orbit determination, attitude determination) and diverse mission contexts (from Earth orbits to space exploration), ENSPACE aims to become a reference low-cost product on the market.

Three years after the project kicked-off, ENSPACE Receiver was integrated in a NASA/Ohio University 3U CubeSat(BOBCAT-1) and deployed from the ISS on the 5th of November 2020, with three main objectives: test the receiver in a real LEO space environment; assess its ability to continuously compute PVT information; and exploit its reconfigurability. Two weeks after its deployment, the ENSPACE receiver successfully computed BOBCAT-1 in-orbit first positions, combining GPS and Galileo signals. While the ENSPACE project has now come to an end, space experimentation and operations continue, including GNSS positioning with ground Assistance Data and the validation of the receiver's Attitude Determination, POD and Authentication algorithms.

In addition to the physical deployment of the receiver in space, the ENSPACE project has set up an innovative test platform, offering multiple experimentation possibilities for innovative space concepts and Galileo added-value. The platform was especially used to demonstrate the capability of the software-defined radio ENSPACE receiver, which was able to track the signal of the Spirent constellation simulator and to propose a real-time multi-constellation PVT solution in multiple space scenarios. In 2021, the ENSPACE receiver has a Technology Readiness Level (TRL) of 7 (i.e. a system prototype demonstration in operational environment). On the market it will take the commercial name of QN400.

With the GEYSER (Galileo cyber Space Receiver) project, Qascom and its consortium are committed to follow in ENSPACE footsteps.

GEYSER complements developments over the past few years with new added-value functionalities, with the objective to become a close-to-market space receiver, and compatible with COTS. Targeting new applications (e.g. cybersecurity and robust PNT, dual-frequency POD for station keeping and collision avoidance, high dynamics navigation, etc.), the GEYSER project aims for new technological development targets, both on software and hardware levels.

In-orbit satellite (IoS) servicing refers to the refuelling or the repairing of space satellites while in orbit. Although considered since the early days of spaceflights, the recent easier access to LEOs and space debris-related issues has generated a renewed interest for the practice.

IoS has the potential to open-up new opportunities through satellite life extension, robotics and salvage, while also offering sustainability benefits through debris removal and material recycling over the longer term. While GNSS could be used as a mean of absolute (for the approach) and relative (for the connection) positioning, it is also suggested

that IoS services may go beyond life extension and up to service enhancement, by providing additional capabilities to the client satellite (e.g. equip an already flying satellite with a new piece of hardware, such as a GNSS receiver).

The characterization of an interoperable GNSS Space Service Volume (SSV) - which is an important enabler for new missions and a key driver for new technological developments - is today limited to Earth orbits up to an altitude of 36,000 km (i.e. GEO). Yet, navigation is also a key technological enabler for cislunar and lunar volume discovery, and all the moon exploration missions that define the emerging lunar economy share similar navigation needs. The international space community plans therefore to extend GNSS PNT applications up to the Moon. Different phases could be considered, starting with the use of the already existing Earth- GNSS constellations via high-sensitivity space receivers, leveraging the use of GNSS signal side lobes. Yet, such approach only allows to reach cislunar areas (not occulted by the Moon). Plus, if the objective is to get enough accuracy and availability to enable autonomous landing and rover guidance, Earth GNSS signals alone are not sufficient.

Therefore possible to consider that Earth-GNSS constellations may be augmented with dedicated lunar orbiting satellites and lunar beacon ranging sources, marking a gradual deployment leading to a full autonomous lunar navigation system. Beyond the primary navigation purpose of such an ambitious system, any other GNSS-based applications could also be considered, such as the study of lunar soil deformation based on GNSS-R [2].

Currently, a number of "traditional" applications of global navigation satellite systems (GNSS) have emerged:

- services on mobile devices for a wide range of consumers - car navigators, navigators for walking man, fitness trackers, taxis, etc.;
- personal navigation (smartphones or specialized trackers);
- transport telematics (M2M) - monitoring of vehicles (movement control, fuel control, monitoring of various telemetry);
- navigation support of various moving objects (land transport, air and water craft);
- tasks requiring high-precision positioning (geodesy, cartography, monitoring of structures, coordinate farming, etc.);
- emergency response systems in case of accidents;
- military tasks and others.

There are new applications of GNSS. This is due to the "digitization" of the economy, production and all areas of our life [14, 18].

The GNSS positioning results are used in:

- automation of production, performance of works and provision of services;
- accounting of work performed and services rendered.

GNSS positioning penetrates into various information systems (personnel management, enterprise, accounting).

There are problems of seamless navigation and the use of combined positioning methods.

When solving problems of transport telematics, there are problems of monitoring new types of objects, as well as monitoring and control of an extended set of object parameters (which is especially important for special equipment).

Several new applications of GNSS technology:

- Employee monitoring system in the "Outdoor & Indoor" mode;
- Car monitoring system on the territory of the maintenance station;
- Monitoring system for performers at the airport;
- Monitoring of floating signs;
- Evaluation of driving styles.

The quality of a tourist trip depends on many factors, for example, GPS navigation and one of the essential is route consistency [19-21]. This geographical factor influences the popularity, efficiency and tourist travel safety. Considering usefulness of reference routes for the sports tourism development, one can assume their feasibility at the present time, when the goals of tourism, its organization system, and geographical directions of tourist flows are changing sharply.

Including 5G as a technology has the potential to have wide-ranging effects on the V2X ecosystem. To take full advantage of its capabilities, operators and industry leaders must familiarize themselves with the tools that modern cellular networks provide and understand how these tools can best be applied in end-to-end solutions [22-25].

V. CONCLUSION

The diversification and the expansion of space users is of great interest to the spaceborne GNSS receivers market. Yet, the consequence it has on the space environment raises the question of the awareness system and traffic management policies it requires. NewSpace activities could indeed overwhelm current space flight safety processes, putting at risk space infrastructure and human spaceflight. Currently, no 'highway code' has been established in outer space by the international community.

Today, space traffic is mainly 'ruled' by the Outer Space Treaty - establishing that no nation may claim sovereignty over outer space (article II) - and the IADC space debris guidelines, that aim to limit the generation of space debris. This is and will therefore remain an international concern. Cooperation - on a global scale - offers an unprecedented opportunity to enhance the safety of active satellites, in order to preserve space operations and all the benefits it brings to the global economy and society. But although the enforcement of Space Traffic Management (STM) policies may soon become inevitable, its implementation is

extremely complex for political (no sovereignty over outer space) and practical reasons.

Tracking potential collisions, notifying impacted parties and coordinating how they respond is still a largely manual process, which is not sustainable as the number of satellites grows. In the past, developing automated systems for a handful of satellites making a few avoidance measures a year was not worth the investment. Today, with the influx of new LEO satellites, handling avoidance measures manually no longer makes economic sense.

Paving the way towards the building of an international approach to STM, the European Commission has recently launched a new 'EU strategy for Space Traffic Management (STM)' flagship project. As announced in the Action Plan on Synergies between Civil, Defence and Space Industries, the project aims to develop STM rules and best practices, limiting the risk that non-EU standards become the norm and supporting the EU in its efforts to achieve technological sovereignty.

The question of the role GNSS solutions could play in this long-lasting process is legitimate. Traffic management requires a good knowledge of each vehicle positioning and attitude, based on standardised and robust technological solutions. The development of spaceborne GNSS receivers and their deployment at a wider scale could therefore be one of the building blocks toward future space regulations. These moreover must be formulated and implemented in the very short term to ensure both space users can safely operate their systems and terrestrial users can benefit from their associated critical services (e.g. navigation, telecommunication, etc.).

REFERENCES

1. <https://earsc.org/wp-content/uploads/2021/10/EARSC-Industry-survey-2021.pdf>
2. Inside GNSS, December 2020. <https://insidegnss.m/ across-the-lunar-landscape-towards-a-dedicated-lunar-pnt-system>.
3. EUSPA EO and GNSS Market Report. Issue 1, 2022.
4. <https://www.gsa.europa.eu/enhanced-navigation-space>.
5. O. V. Varlamov, "Organization of single frequency DRM digital radio broadcasting networks. Features and results of practical tests," *2018 Systems of Signal Synchronization, Generating and Processing in Telecommunications (SYNCHROINFO)*, Minsk, 2018, pp. 1-8. DOI: 10.1109/SYNCHROINFO.2018.8456925
6. O. V. Varlamov and Abi Assali Bychkova A. Development of a DRM standard digital simultaneous radio broadcasting network for Venezuela. *REDS: Telecommunication devices and systems*. 2020. Vol. 10. No. 2, pp. 23-27.
7. O. V. Varlamov and A. A. Bychkova, "Basis of Technical Design and Development a Single-Frequency

- DRM Digital Broadcasting Network for Venezuela," *2021 Systems of Signal Synchronization, Generating and Processing in Telecommunications (SYNCHROINFO)*, 2021, pp. 1-7, doi: 10.1109/SYNCHROINFO51390.2021.9488396.
8. O.V. Varlamov, "Organization of single frequency DRM digital radio broadcasting networks. Features and results of practical tests", *T-Comm*, vol. 12, no. 11, pp. 4-20, 2018.
9. O. V. Varlamov and V. O. Varlamov, "Distribution of maximum levels of atmospheric radio noise in LF and MF ranges in the territory of the Earth", *H&ES Research*, vol. 9, no. 5, pp. 42-51, 2017.
10. O.V. Varlamov, V.O. Varlamov and A.V. Dolgopyatova, "DRM broadcasting international network to create an information field in the Arctic region", *T-Comm*, vol. 13, no. 9, pp. 9-16, 2019.
11. V. M. J. D. Santos and Y. A. Kovagin, "Building digital broadcasting networking in the low and midium frequencies", *T-Comm*, vol. 13, no. 4, pp. 55-63, 2019.
12. O. V. Varlamov, "Experimental Study of a Synchronous DVB-T2 Network in the Yaroslavl Region. Problems with Some Manufacturers' Receivers," *2020 International Conference on Engineering Management of Communication and Technology (EMCTECH)*, Vienna, Austria, 2020, pp. 1-4, doi: 10.1109/EMCTECH49634.2020.9261562.
13. A. V. Dolgopyatova and O. V. Varlamov, "Analysis of Long-Range VHF Radio Waves Propagation to Specify Protection Ratios Between Coexisting DRM+, RAVIS and IBOC Systems," *2021 Systems of Signal Synchronization, Generating and Processing in Telecommunications (SYNCHROINFO)*, 2021, pp. 1-4, doi: 10.1109/SYNCHROINFO51390.2021.9488392.
14. S. A. Platonov, A. V. Platonov, M. E. Postnikov, S. V. Khadonova and S. S. Dymkova, "Using Global Navigation Satellite Systems to Solve Complex Application Problems," *2019 Systems of Signals Generating and Processing in the Field of on Board Communications*, Moscow, Russia, 2019, pp. 1-8. DOI: 10.1109/SOSG.2019.8706807
15. S. S. Dymkova, "Conjunction and synchronization methods of earth satellite images with local cartographic data," *2020 Systems of Signals Generating and Processing in the Field of on Board Communications*, Moscow, Russia, 2020, pp. 1-7, doi: 10.1109/IEEECONF48371.2020.9078561.
16. S. V. Khadonova, A. V. Ufimtsev and S. S. Dymkova, "Wide application innovative monitoring system with personal smart devices," *2020 Systems of Signal Synchronization, Generating and Processing in Telecommunications (SYNCHROINFO)*, Svetlogorsk, Russia, 2020, pp. 1-5, doi: 10.1109/SYNCHROINFO49631.2020.9166115.
17. S. S. Dymkova and A. D. Dymkov, "Synchronizing of moving object with novel 3D maps imaging," *2020 Systems of Signal Synchronization, Generating and Processing in Telecommunications (SYNCHROINFO)*, Svetlogorsk, Russia, 2020, pp. 1-5, doi: 10.1109/SYNCHROINFO49631.2020.9166029.
18. S. V. Khadonova, A. V. Ufimtsev and S. S. Dymkova, "'Digital Smart Airport" System Based on Innovative Navigation and Information Technologies," *2020 International Conference on Engineering Management of Communication and Technology (EMCTECH)*, Vienna, Austria, 2020, pp. 1-6, doi: 10.1109/EMCTECH49634.2020.9261529.
19. S. S. Dymkova and A. D. Dymkov, "Multifactorial methodology of cycling routes time calculation based on 3D maps," *2021 Systems of Signals Generating and Processing in the Field of on Board Communications*, 2021, pp. 1-8, doi: 10.1109/IEEECONF51389.2021.9416046.
20. S. S. Dymkova and A. D. Dymkov, "Experimental Studies of GNSS Errors in Rough and Wooded Mountainous Terrain," *2021 International Conference on Engineering Management of Communication and Technology (EMCTECH)*, 2021, pp. 1-6, doi: 10.1109/EMCTECH53459.2021.9619169.
21. S. Dymkova, "Applicability of 5G subscriber equipment and global navigation satellite systems", *Synchroinfo Journal*, vol. 7, no. 5, pp. 36-48, 2021. DOI: 10.36724/2664-066X-2021-7-5-36-48
22. S. S. Dymkova, "Breakthrough 5G data call using dynamic spectrum sharing to accelerate nationwide 5G deployments", *Synchroinfo Journal*, vol. 5, no. 6, pp. 17-21, 2019.
23. S. S. Dymkova, "Cloud IoT platforms and apps for optimized transport management," *REDS: Telecommunication devices and systems*. Vol. 10. No. 4, pp. 39-50.
24. V. O. Tikhvinsky. The fifth element of the mobile world: the results of MWC-17. *T-Comm*. 2017. Vol. 11. No. 3, pp. 4-11.
25. G. A. Fokin. 5G network positioning and statistic models for its accuracy evaluation. *T-Comm*, 2020, vol. 14, no.12, pp. 4-17.

Advisory Board Announced



Geo Week Advisory Board set to help craft programming, recommend speakers, and deliver critical insights to geospatial and built world professionals.

Organizers of Geo Week, the premier event that champions the coming together of geospatial technologies and the built world, have announced an impressive list of influential leaders within the geospatial and built world industries who will be participating on the 2023 event's Advisory Board. The 2023 event will take place February 13-15, 2023 in Denver, Colorado.

"By bringing together professionals across verticals and disciplines, the 2023 Advisory Board will address the most pressing issues facing the geospatial, 3D and built world environments today," said Lee Corkhill, Group Director at Diversified Communications, organizer of the event. "Board members are at the top of their fields, and they are committed to delivering the best conference and expo the geospatial and built markets have ever seen."

Members of the 2023 Advisory Board include:

- Dr. Qassim Abdullah, Woolpert, Inc.
- Ashley Chappell, NAA
- Kelly Cone, ClearEdge3
- Kevin Dowling, Kaart
- Martin Flood, GeoCue Group
- Birgitta Foster, Sandia National Laboratories
- Thomas Haun, Turner Staffing Group
- Kouros Langari, Caltran
- Amar Niyegandhi, Dewberry

- Lindsay Prichard-Fox, TiverBuilt
- Barbara Ryan, World Geospatial Industry Council (WGIC)
- Scott Simmons, Open Geospatial Consortium
- Dr. Jason Stoker, U.S. Geological Survey (USGS)
- Daniel Stonecipher, Schneider Electric
- Dr. Stewart Walker, LIDAR Magazine
- Jennifer Wozencraft, US Army Corps of Engineers
- Geoff Zeiss, Between the Poles

Bios can be found here.

The Advisory Board will assist in developing conference programming comprised of both general sessions and breakout sessions that delve into the full spectrum of data needs, work processes, software integration and standards in both the geospatial and BIM worlds. Specific vertical industries include architecture, engineering, & construction; asset & facility management; disaster & emergency response; earth observation & satellite applications; energy & utilities; infrastructure & transportation; land & natural resource management; mining & aggregates; surveying & mapping; and urban planning / smart cities.

"Geo Week is such an important event to attend for everybody in the 3D reality capture market," said Martin Flood, Vice President Special Projects at GeoCue Group. "From its roots in the earliest days of commercial lidar mapping technology to today's combined conference and tradeshow covering innovations, advances and the growing convergence of 3D mapping technologies across multiple sectors and applications, it really is a 'can't miss' event."

Kevin Dowling, Chief Executive Office of Kaarta, agreed, stating that "Geo Week represents not just the convergence of all things geospatial but the emergence of many new applications that turn spatial data and sensor information into opportunities for cities, businesses, and organizations to better capture, understand, and deploy this information to radically improve understanding and planning of resources."

The digital transformation of our world is a growing and urgent need. Kourosh Langari, BIM Manager at Caltrans reiterates this statement when saying "it is difficult to say where technology will be in the future, but what we can predict is that from conception to construction, your project will be virtually available to all concerned stakeholders."

The Advisory Board is responsible for recommending conference topics and speakers, reviewing submitted abstracts, consulting on the program, and acting as a resource to develop different aspects of the event. In 2023, the Geo Week conference program will showcase real-world use cases and highlight emerging trends in technology and processes. In addition to the extensive conference program, Geo Week offers a vendor-neutral show floor featuring the newest geospatial and built world products and solutions to qualify and compare.

Registration will open in October. Geospatial and built world professionals are encouraged to register early to secure discounted conference pricing, and to fill out the Attendee Inquiry form for event updates.

About Geo Week

Geo Week is part of a network of events and media for the global geospatial and built markets organized by Diversified Communications, a leading organizer of conferences, trade shows, and online media with 16 years in the technology arena. Geo Week, taking place February 13-15, 2023, reflects the increased integration between the built environment, advanced airborne/terrestrial technologies, and commercial 3D technologies. Powerful partnership events will also take place at Geo Week, including ASPRS (American Society for Photogrammetry and Remote Sensing) Annual Conference.

Diversified Communications also produces Lidar & Geospatial Newsletter, 3D Technology Newsletter, AEC Innovations Newsletter, GeoBusiness Show (UK), Digital Construction Week (UK), Commercial UAV Expo and Commercial UAV News. For more information, visit www.geo-week.com.



The United Nations specialized agency for information and communication technologies

القراءة بالعربية | 中文阅读 | Leer en español |
Lire en français | Читать по русски

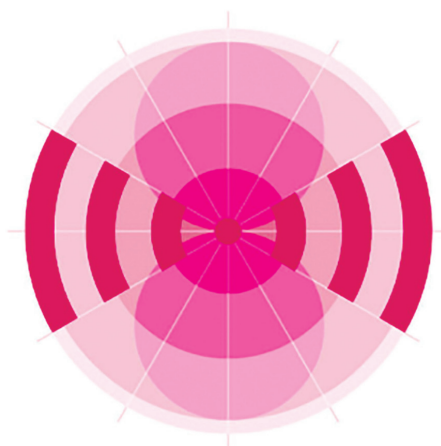
MEDIA ADVISORY

30TH ITU WORLD
RADIOCOMMUNICATION SEMINAR

ITUWRS
GENEVA2022

24 - 28 October
Geneva, Switzerland

www.itu.int/go/wrs-22
#ITURRS



CONNECTIVITY UNLEASHED

2022 Report
28 February – 03 March

An Event of



#MWC22

